Mon. Not. R. Astron. Soc. **000**, 000–000 (0000) Printed 7 May 2014 (MN LATEX style file v2.2)

The visibility of Lyman Alpha Emitters: constraining reionization, ionizing photon escape fractions and dust

Anne Hutter[1⋆], Pratika Dayal[2], Adrian M. Partl[1], Volker Müller[1]
[1] *Leibniz-Institut für Astrophysik, An der Sternwarte 16, 14482 Potsdam, Germany*
[2] *SUPA†, Institute for Astronomy, University of Edinburgh, Royal Observatory, Edinburgh, EH9 3HJ, UK*

arXiv:1401.2830v2 [astro-ph.CO] 6 May 2014

ABSTRACT
We build a physical model for high-redshift Lyman Alpha emitters (LAEs) by coupling state of the art cosmological simulations (GADGET-2) with a dust model and a radiative transfer code (pCRASH). We post-process the cosmological simulation with pCRASH using five different values of the escape fraction of hydrogen ionizing photons ($f_{\rm esc} = 0.05, 0.25, 0.5, 0.75, 0.95$) until reionization is complete, i.e. the average neutral hydrogen fraction drops to $\langle \chi_{HI} \rangle \simeq 10^{-4}$. Then, the only free-parameter left to match model results to the observed Lyα and UV luminosity functions of LAEs at $z \simeq 6.6$ is the relative escape of Lyman Alpha (Lyα) and continuum photons from the galactic environment (f_α/f_c). We find a *three-dimensional* degeneracy such that the theoretical model can be reconciled with observations for an IGM Lyα transmission $\langle T_\alpha \rangle_{LAE} \simeq 38 - 50\%$ (which translates to $\langle \chi_{HI} \rangle \simeq 0.5 - 10^{-4}$ for Gaussian emission lines), $f_{\rm esc} \simeq 0.05 - 0.50$ and $f_\alpha/f_c \simeq 0.6 - 1.8$.

Key words: radiative transfer - methods: numerical - ISM: dust, extinction - cosmology: dark ages, reionization - galaxies: high-redshift, luminosity function

1 INTRODUCTION

The Epoch of Reionization (EoR) begins when the first stars start producing neutral hydrogen (H I) ionizing photons, carving out an ionized Strömgren region in the neutral intergalactic medium (IGM) around themselves, and ends when all the H I in the IGM is ionized. Understanding the process of cosmic reionization is extremely important because in addition to marking the last major change in the ionization state of the Universe, it affected all subsequent structure formation through a number of radiative feedback effects (see e.g. Barkana & Loeb 2001; Ciardi & Ferrara 2005; Maio et al. 2011; Sobacchi & Mesinger 2013; Wyithe & Loeb 2013, and references therein). A broad picture that has emerged (Choudhury & Ferrara 2007) is one wherein hydrogen reionization is an extended process that starts at $z \approx 15$ and is about 90% complete by $z \simeq 8$; while it is initially driven by metal-free Population III stars in low-mass halos ($\leqslant 10^8 {\rm M}_\odot$), the conditions for star formation in these halos are soon erased by a combination of chemical and radiative feedback by $z \simeq 10$. However, any attempt at modelling reionization necessarily requires a number of important assumptions regarding the number of H I ionizing photons produced by the source galaxy population depending on their physical properties, the fraction of these photons ($f_{\rm esc}$) that can escape out of the galactic environment and contribute to reionization, and the clumping factor of the IGM at high-redshifts, to name a few (Salvaterra et al. 2011). Given these assumptions, reionization scenarios need to be constantly updated as new data sets are acquired.

By virtue of their continually growing numbers, a valuable new data set is provided by high-redshift Lyman Alpha Emitters (LAEs); this is a class of galaxies identified by means of their Lyman Alpha (Lyα) emission line at 1216 Å in the galaxy rest-frame. Indeed, hundreds of LAEs have now been confirmed in the epoch of reionization: $z \simeq 5.7$ (Malhotra et al. 2005; Shimasaku et al. 2006; Hu et al. 2010; Curtis-Lake et al. 2012), $z \simeq 6.6$ (Taniguchi et al. 2005; Kashikawa et al. 2006; Hu et al. 2010; Ouchi et al. 2010; Kashikawa et al. 2011) and $z \simeq 7$ (Iye et al. 2006; Ouchi et al. 2009; Stark et al. 2010; Pentericci et al. 2011). In addition to their number statistics, LAEs have been rapidly gaining popularity as probes of reionization and high-redshift galaxy evolution for two reasons: (a) the strength, width and continuum break bluewards of the Lyα line makes their detection unambiguous, and (b) Lyα pho-

⋆ E-mail:ahutter@aip.de
† Scottish Universities Physics Alliance

© 0000 RAS

tons are extremely sensitive to attenuation by H I ; the observed Lyα luminosity can then be used to infer the ionization state of the IGM at redshifts close to those of the emitter and hence to reconstruct, at least piecewise, the cosmic reionization history.

However, interpreting LAE data is complicated by a number of physical effects. First, the intrinsic Lyα luminosity depends on the total number of H I ionizing photons that are produced by a galaxy, depending on the star formation rate (SFR), age and metallicity of its stellar population (e.g. Santos 2004). Second, depending on the H I and dust contents in the interstellar medium (ISM), only a fraction $(1-f_{\rm esc})$ of these H I ionizing photons are able to contribute to the intrinsic Lyα luminosity by ionizing the ISM H I ; the rest contribute to building the ionized H II region around the galaxy. We briefly digress to note that the dependence of $f_{\rm esc}$ on galaxy properties has been the subject of much recent debate: while some authors find $f_{\rm esc}$ to decrease with an increase in the halo mass (Razoumov & Sommer-Larsen 2010; Yajima et al. 2011; Ferrara & Loeb 2013), other works find the opposite trend (Gnedin et al. 2008; Wise & Cen 2009). The value of $f_{\rm esc}$ also remains poorly constrained with findings ranging from a few percent (e.g. Gnedin et al. 2008) up to $20-30\%$ (e.g. Mitra et al. 2013) or even higher (e.g. Wise & Cen 2009). Third, only a fraction (f_α) of the Lyα photons produced inside a galaxy can escape out of it unattenuated by dust (Dayal et al. 2008; Finkelstein et al. 2009; Nagamine et al. 2010; Forero-Romero et al. 2011; Dayal & Ferrara 2012). Fourth, only a fraction (T_α) of the Lyα photons that emerge out of a galaxy are transmitted through the IGM and reach the observer. As expected, this transmission sensitively depends on the IGM H I ionization state and it has been shown that only galaxies residing in over-lapping H II regions would be observed as LAEs in the initial stages of reionization, i.e. reionization increases the observed clustering of LAEs (McQuinn et al. 2007b; Dayal et al. 2009). Fifth, the Lyα IGM transmission calculation is complicated by the presence of peculiar velocities. Inflows (outflows) of gas into (from) the emitter blue-shift (red-shift) the Lyα line, leading to a decrease (increase) in the value of T_α along different lines of sight, strongly affecting the visibility of galaxies as LAEs (Verhamme et al. 2006; Iliev et al. 2008; Zheng et al. 2010; Dijkstra et al. 2011). Indeed, Santos (2004) has shown that the IGM ionization state can not be constrained in the presence of peculiar velocities. However, Dayal et al. (2011) have shown that the interpretation of LAE data is much more involved; a decrease in the Lyα transmission due to peculiar velocities and/or a highly neutral IGM can be compensated by an increase in f_α due to dust being clumped in the ISM of LAEs, as per the 'Neufeld-model' (Neufeld 1991).

A number of past theoretical works have used one or more of the above ingredients to use LAEs as tracers of reionization. With semi-analytic modelling, a number of authors (e.g. Dijkstra et al. 2007; Dayal et al. 2008; Samui et al. 2009) have shown that the LAE Lyα luminosity functions (LFs) are consistent with a fully ionized IGM and can be explained solely by an evolution of the underlying dark matter halo mass functions. However, when considered in combination with the non-evolving observed ultraviolet (UV) LFs of LAEs between $z \simeq 5.7$ and 6.6 (Kashikawa et al. 2006), some of these works (Dijkstra et al. 2007; Ouchi et al. 2010) argue for an additional dimming of the Lyα line by about 30%. A number of studies have used large pure dark matter simulations to study the clustering of LAEs (McQuinn et al. 2007a; Iliev et al. 2008; Orsi et al. 2008). Finally, a number of studies have been undertaken using cosmological hydrodynamic simulations with dust (Dayal et al. 2008, 2009; Nagamine et al. 2010; Forero-Romero et al. 2011), with radiative transfer without dust (Zheng et al. 2010) and radiative transfer with dust (Dayal et al. 2011; Forero-Romero et al. 2011; Duval et al. 2014).

This work is quite close in spirit to the calculations presented in Dayal et al. (2011) wherein the authors used (a) cosmological hydrodynamic simulations run with GADGET-2 to obtain the physical properties of $z \simeq 5.7$ galaxies, (b) a dust model that took into account the entire star formation history of each galaxy to calculate its dust enrichment and, (c) a RT code (CRASH) to obtain the ionization fields to calculate the IGM Lyα transmission for each galaxy, in order to identify the simulated galaxies that would be observationally classified as LAEs. Using this model, the authors showed that the effects of dust and IGM are degenerate in affecting the visibility of LAEs such that a large f_α can be compensated by a small T_α and vice versa to yield a given value of the observed Lyα luminosity. However, the main caveat in that work was that the authors used a constant value of $f_{\rm esc} = 0.02$ (Gnedin et al. 2008) for all galaxies in their calculations, and started their RT runs assuming the IGM gas to be in photoionization equilibrium with a uniform ultraviolet background (UVB) produced by unresolved sources corresponding to an average neutral hydrogen fraction, $\langle \chi_{\rm HI} \rangle = 0.3$.

In this work, we substiantially enhance the model presented in Dayal et al. (2011) to build a self-consistent model that couples cosmological SPH simulations, dust modelling and a fast RT code (pCRASH) to identify LAEs without making any prior assumptions on the IGM ionization state, $f_{\rm esc}$ and the ISM dust distribution. Starting from a uniform neutral IGM, consistent with the Haardt & Madau (1996) background imposed in simulations, we use 5 different values of $f_{\rm esc} = 0.05, 0.25, 0.5, 0.75, 0.95$ in order to study how varying $f_{\rm esc}$ affects the visibility of LAEs through: (a) the direct impact on the intrinsic Lyα luminosity, and (b) the IGM Lyα transmission that depends on the topology and extent of H II regions as determined by $f_{\rm esc}$. Comparing the statistics of the simulated LAEs to observations, our aim is to jointly constrain three fundamental parameters that determine the visibility of LAEs - $f_{\rm esc}$, χ_{HI} (or T_α) and the relative escape of Lyα photons with respect to continuum photons from the dusty ISM of galaxies (f_α/f_c).

We begin by describing the hydrodynamical simulation, the dust model and the identification of galaxies as Lyman Break Galaxies (LBG) through the UV continuum in Sec. 2. We follow this approach since UV photons are only attenuated by dust but unaffected by the IGM ionization state, simplifying their identification. In order to validate the sim-

ulations, we compare the simulated LBG UV LFs to observations in Sec. 3; a comparison of the simulated LBG stellar mass functions, stellar mass densities and specific star formation rates with the observations are shown in Appendix A for completeness. Once the physical properties of the simulated galaxies have been validated, we choose a simulation snapshot at the edge of the epoch of reonization ($z \simeq 6.7$) and post-process it with a fast RT code (pCRASH) with the 5 values of $f_{\rm esc}$ mentioned above, as explained in Sec. 4. We then compare the simulated LAE UV and Lyα LFs with observations (Kashikawa et al. 2011) in Sec. 5 in order to jointly constrain $f_{\rm esc}$, χ_{HI} and f_α/f_c. Due to the model dependent relation between χ_{HI} and the Lyα IGM transmission (T_α) we show our constraints also in terms of $f_{\rm esc}$, T_α and f_α/f_c, before concluding in Sec. 6.

2 COSMOLOGICAL HYDRODYNAMIC SIMULATIONS

In this section we describe the cosmological simulation used to obtain the physical properties of high-redshift galaxies and the semi-analytic model used to obtain their dust enrichment, in order to calculate their observed visibility in the UV.

2.1 The simulation

The hydrodynamical simulation analyzed in this work has been carried out using the TreePM-SPH code GADGET-2 (Springel 2005). The adopted cosmological model corresponds to the ΛCDM universe with dark matter (DM), dark energy and baryonic density parameter values of (Ω_Λ, Ω_m, Ω_b) = (0.73, 0.27, 0.047), a Hubble constant $H_0 = 100h = 70{\rm kms}^{-1}{\rm Mpc}^{-1}$, and a normalisation $\sigma_8 = 0.82$, consistent with the results from WMAP5 (Komatsu et al. 2009). The simulation box has a size of $80h^{-1}$ comoving Mpc (cMpc), and contains 1024^3 DM particles, and initially the same number of gas particles; the mass of a DM and gas particle is $3.6\times10^7h^{-1}{\rm M}_\odot$ and $6.3\times10^6h^{-1}{\rm M}_\odot$, respectively. The softening length for the gravitational force is taken to be $3h^{-1}$ comoving kpc and the value of the smoothing length for the SPH kernel for the computation of hydrodynamic forces is allowed to drop at most to the gravitational softening.

The runs include the star formation prescriptions of Springel & Hernquist (2003) such that the ISM is described as an ambient hot gas containing cold clouds, which provide the reservoir for star formation, with the two phases being in pressure equilibrium; the relative number of stars of different masses is computed using the Salpeter initial mass function (IMF; Salpeter 1955) between 0.1-100M$_\odot$. The density of the cold and of the hot phase represents an average over small regions of the ISM, within which individual molecular clouds cannot be resolved by simulations sampling cosmological volumes. The runs also include the feedback model described in Springel & Hernquist (2003) which includes (a) thermal feedback: supernovae (SN) inject entropy into the ISM, heat up nearby particles and destroy molecules, (b) chemical feedback: metals produced by star formation and SN are carried by winds and pollute the ISM, and (c) mechanical feedback: galactic winds powered by SN. In the case of mechanical feedback, the momentum and energy carried away by the winds are calculated assuming that the galactic winds have a fixed velocity of $500\,{\rm km\,s}^{-1}$ with a mass upload rate equal to twice the local star formation rate, and carry away a fixed fraction (50%) of the SN energy (for which the canonical value of 10^{51} ergs is adopted). Finally, the run assumes a metallicity-dependent radiative cooling (Sutherland & Dopita 1993) and a uniform redshift-dependent UV Background (UVB) produced by quasars and galaxies as given by Haardt & Madau (1996).

Galaxies are recognized as gravitationally-bound groups of at least 20 total (DM+gas+star) particles using the Amiga Halo Finder (AHF; Knollmann & Knebe 2009). When compared to the standard Sheth-Tormen mass function (Sheth & Tormen 1999), the simulated mass function is complete for halo masses $M_h \geqslant 10^{9.2}\,{\rm M}_\odot$ for $z \simeq 6-8$; galaxies above this mass cut-off are referred to as the "complete sample". Of this complete sample, we identify all the "resolved" galaxies that contain a minimum of $4N$ gas particles, where $N = 40$ is the number of nearest neighbours used in the SPH computations; this is twice the standard value of $2N$ gas particles needed to obtain reasonable and converging results (e.g. Bate & Burkert 1997). We impose an additional constraint and only use those resolved galaxies that contain at least 10 star particles so as to get a statistical estimate of the composite spectral energy distribution (SED). For each resolved galaxy used in our calculations (with $M_h \geqslant 10^{9.2}\,{\rm M}_\odot$, more than $4N$ gas particles and a minimum of 10 star particles) we obtain the properties of all its star particles, including the redshift of, and mass/metallicity at formation; we also compute global properties including the total stellar mass (M_*), gas mass (M_g), DM mass (M_h), mass-weighted stellar metallicity (Z_*) and the mass weighted stellar age (t_*).

2.2 Dust model

The evidence for dust at high-redshifts comes from observations of damped Lyα systems (Pettini et al. 1994; Ledoux et al. 2002) and from the thermal dust emission from SDSS QSOs (Omont et al. 2001; Bertoldi & Cox 2002). Although dust is produced both by SN and evolved stars, several works (Todini & Ferrara 2001; Dwek et al. 2007) have shown that the contribution of AGBs to the total dust content is negligible at $z \gtrsim 6$, since the age of the Universe is shorter than the typical evolutionary timescales of AGBs above this redshift. We therefore make the hypothesis that Type II SN (SNII) are the primary dust factories and compute the total dust mass, M_d in each of our simulated galaxies as described in Dayal et al. (2010).

This dust mass can be used to obtain the total optical depth, τ_c, to continuum photons as

$$\tau_c = \frac{3\Sigma_d}{4as}, \quad (1)$$

where $\Sigma_d = M_d[\pi r_d^2]^{-1}$ is the dust surface mass density, r_d is the dust distribution radius, $a = 0.05\mu m$

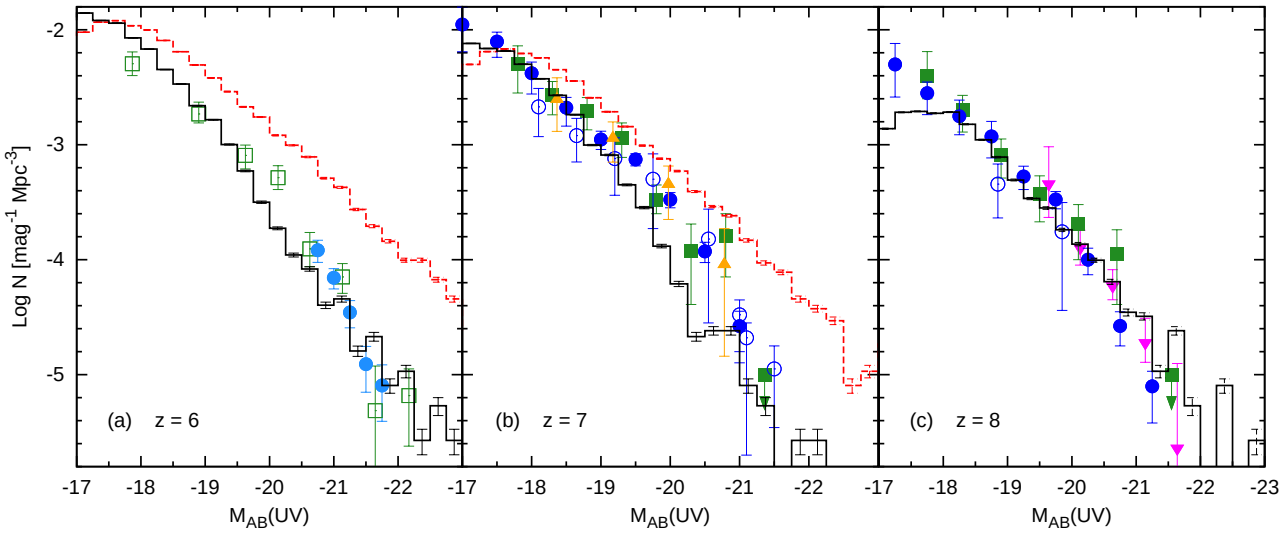

Figure 1. UV luminosity functions at $z \simeq 6, 7$ and 8, from left to right, as marked in each panel. In all panels, the solid black (dashed red) histograms show the dust corrected (intrinsic) simulated UV LFs with error bars showing the Poissonians error and symbols showing the observed data. The observed UV LFs have been taken from (a) $z \simeq 6$: Bouwens et al. (2007, empty squares), McLure et al. (2009, filled circles); (b) $z \simeq 7$: Bouwens et al. (2011, filled squares), McLure et al. (2010, empty circles), McLure et al. (2013, filled circles), Oesch et al. (2010, filled triangles) and (c) $z \simeq 8$: Bradley et al. (2012, filled triangles), Bouwens et al. (2011, filled squares), McLure et al. (2010, empty circles) and McLure et al. (2013, filled circles).

and $s = 2.25\,\mathrm{g\,cm^{-3}}$ are the radius and material density of graphite/carbonaceous grains, respectively (Todini & Ferrara 2001). Since in our model dust and gas are assumed to be perfectly mixed, the dust distribution radius is taken to be equal to the gas distribution radius $r_g = 4.5\lambda r_{vir}$ where the spin parameter (λ) has a value of about 0.04 averaged across the galaxy population studied (Barnes & Efstathiou 1987; Steinmetz & Bartelmann 1995; Ferrara et al. 2000) and r_{vir} is the virial radius, calculated assuming the collapsed region has an overdensity of 200 times the critical density. This dust optical depth can then be used to obtain the escape fraction of UV photons (f_c) assuming a screen-like dust distribution such that $f_c = e^{-\tau_c}$.

2.3 Identifying Lyman Break Galaxies

To identify the simulated galaxies that could be observed as LBGs at $z \simeq 6-8$, we start by computing their UV luminosities. We consider each star particle to form in a burst, after which it evolves passively. The total SED, including both the stellar and nebular continuum, is computed for each star particle via the population synthesis code `STARBURST99` (Leitherer et al. 1999), using its mass, stellar metallicity and age. The total intrinsic UV luminosity, L_c^{int} (at 1500 Å in the galaxy rest frame) is then calculated for each progenitor by summing the SEDs of all its star particles.

Continuum photons can be absorbed by dust within the ISM and only a fraction, f_c, escape out of any galaxy unattenuated by dust. However, these photons are unaffected by the ionization state of the IGM, and all the continuum photons that escape out of a galaxy can then reach the observer, so that the observed continuum luminosity can be expressed as $L_c^{obs} = L_c^{int} \times f_c$; this can be translated into an absolute magnitude, M_{UV}. In accordance with current observational criterion, at each redshift $z \simeq 6-8$, resolved simulated galaxies with $M_{UV} \leqslant -17$ are identified as LBGs.

3 COMPARING THE SIMULATIONS WITH LBG OBSERVATIONS

Once we have identified the simulated galaxies that would be detected as LBGs in the snapshots at $z \simeq 6-8$, we compare their UV LFs, stellar mass functions, stellar mass densities (SMD) and specific star formation rates (sSFR) to the observed values in order to validate the simulations used in this work. In this section we show a comparison between the intrinsic and dust-attenuated (observed) theoretical UV LFs and the data. The theoretical stellar mass functions, SMD and sSFR, and their comparison with observed values are shown in Appendix A.

We calculate the intrinsic UV LFs by binning simulated LBGs on the basis of their intrinsic (i.e. dust-unattenuated) UV magnitudes and dividing this by the width of the UV bin (0.5 dex), and the volume of the box. We find that the intrinsic UV LF shifts towards brighter luminosities and higher number densities with decreasing redshift from $z \simeq 8$ to 6, as expected from the hierarchical structure formation scenario where successively larger systems build up with time from the merger of smaller systems. As seen in Fig. 1, we find that the simulated intrinsic LBG UV LFs are over-estimated with respect to the data, with the over-estimation increas-

ing with decreasing redshift, hinting at the increasing dust enrichment of these galaxies; we note that the intrinsic UV LF at $z \simeq 8$ is already in agreement with the observations, requiring no dust correction at this redshift.

We then use the observed (i.e. dust attenuated) UV luminosity obtained for each galaxy at $z \simeq 6-8$ (see Secs. 2.2 and 2.3) to build the observed UV LF. It is encouraging to note that both the slope and the amplitude of the dust attenuated simulated LFs are in agreement with the observations for $z \simeq 6$ and 7 as seen from Fig. 1; as mentioned before, the simulated UV LF at $z \simeq 8$ requires no dust to match the observations. As can be seen from the same figure, the effects of dust on continuum photons at $z \simeq 6, 7$ are most severe for the most massive/luminous galaxies; indeed while $f_c \simeq 0.8$ for galaxies in halo masses of $M_h \leqslant 10^{10}\mathrm{M}_{\odot}$, the value drops steadily thereafter such that $f_c \simeq 0.01$ for the largest galaxies at both $z \simeq 6, 7$. Further, as a result of galaxies typically being less massive, younger, and hence less dust enriched with increasing redshift, averaged over all LBGs f_c drops from $\simeq 1$ at $z \simeq 8$ to 0.6 at $z \simeq 7$ and 0.5 at $z \simeq 6$. We briefly digress to note that these average f_c values are about a factor of two higher than the values inferred in Dayal et al. (2010). This is due to the different feedback models implemented in these two simulations: while only 25% of the SN energy was used to power outflows in the simulation used in Dayal et al. (2010), 50% of the SN energy has been used to power outflows in the simulation used in this work. As a result of the much larger energy inputs that power SN winds in driving out gas from the galaxy, the typical stellar masses and SFRs obtained from the simulation used in this work are about a factor two lower than those presented in Dayal et al. (2010).

Returning to our discussion regarding the observed LBG UV LFs, we notice that these also shift to progressively higher luminosities and/or higher number densities with decreasing redshift. Dayal et al. (2013) have shown that this evolution depends on the luminosity range probed: the steady brightening of the bright end of the LF is driven by genuine physical luminosity evolution due to a fairly steady increase in the UV luminosity (and hence star-formation rates) in the most massive LBGs; the evolution at the faint end arises due to a mixture of both positive and negative luminosity and density evolution as these putative systems brighten and fade, and continuously form and merge into larger systems.

Finally, we find that the best fit Schechter parameters to the dust attenuated simulated UV LFs are: faint end slope $\alpha = (-1.9\pm0.2, -2.0\pm0.2, -1.8\pm0.2)$ and the knee of the luminosity function $M_{UV,*} = (-19.8\pm0.3, -19.7\pm0.2, -19.9\pm 0.3)$ at $z \simeq (6, 7, 8)$. These values are in agreement with the values $\alpha = (-1.71 \pm 0.11, -1.90 \pm 0.14, -2.02 \pm 0.22)$, $M_{UV,*} = (-20.04 \pm 0.12, -19.9 \pm 0.2, -20.12 \pm 0.37)$ and $\alpha = (-1.74 \pm 0.16, -2.01 \pm 0.21, -1.91 \pm 0.32)$, $M_{UV,*} = (-20.24 \pm 0.19, -20.14 \pm 0.26, -20.1 \pm 0.52)$ inferred observationally by McLure et al. (2009, 2013) and Bouwens et al. (2011) at $z \simeq (6, 7, 8)$, respectively.

4 SIMULATING LAES

In the previous section (and Appendix A), we have validated that the simulated galaxy population at $z \simeq 6-8$ is in agreement with a number of high-z LBG observations. We now use these galaxy populations to identify the simulated galaxies that could be detected as LAEs. We start by describing the radiative transfer code (pCRASH) used to obtain reionization topologies for $f_{\rm esc} = 0.05, 0.25, 0.5, 0.75, 0.95$, which are utilized to calculate the IGM Lyα transmission. We then describe how these transmission values, and the effects of dust on Lyα photons are taken into account, so as to obtain the observed Lyα luminosity from the intrinsic value for each galaxy. We note that all the radiative transfer and Lyα calculations are carried out using a single snapshot of the hydrodynamical simulation at the edge of the reionization epoch, at $z \simeq 6.7$.

4.1 Reionizing the Universe with pCRASH

As mentioned in Sec. 1, the progress of reionization critically depends on the total number of H I ionizing photons that can escape a galaxy and ionize the IGM around it. As expected, this depends both on the total number of H I ionizing photons produced by a galaxy, as well as the fraction that can escape the galactic environment ($f_{\rm esc}$). While the simulated star formation rates are in reasonable agreement with observations (see Appendix A), giving us a handle on the H I ionizing photon production rate, the value of $f_{\rm esc}$ remains only poorly understood: using a variety of theoretical models, the value of $f_{\rm esc}$ has been found to range between $0.01 - 0.8$ (see e.g. Ricotti & Shull 2000; Fujita et al. 2003; Razoumov & Sommer-Larsen 2006; Wise & Cen 2009).

Due to the poor theoretical constraints available on the value of $f_{\rm esc}$, we do not make any prior assumptions on its value. We instead post-process the hydrodynamical simulation snapshot at $z \simeq 6.7$ with the radiative transfer code pCRASH using five different values of $f_{\rm esc} = 0.05$, 0.25, 0.50, 0.75 and 0.95 to study how varying $f_{\rm esc}$ affects the progress of reionization.

We now briefly describe pCRASH and interested readers are referred to Ciardi et al. (2001), Maselli et al. (2003, 2009) and Partl et al. (2011) for more details. pCRASH is a 3D grid-based MPI-parallelized radiative transfer code that utilizes a combination of ray tracing and Monte Carlo schemes. It follows the time evolution of the IGM gas properties including ionization fractions (H I and He I , He II) and the temperature. A large number of point sources with different spectra emit photon packages into the medium. The relevant matter-radiation interactions (photoionization, recombination, collisional ionization) as well as the heating/cooling of the IGM (collisional ionization cooling, recombination cooling, collisional excitation cooling, bremsstrahlung, Compton cooling/heating, adiabatic cooling, photoheating) are calculated. In addition, the code includes diffuse radiation following recombinations of ionized atoms. For the radiative transfer runs, we use the density and temperature fields obtained from the $z \simeq 6.7$ snap-

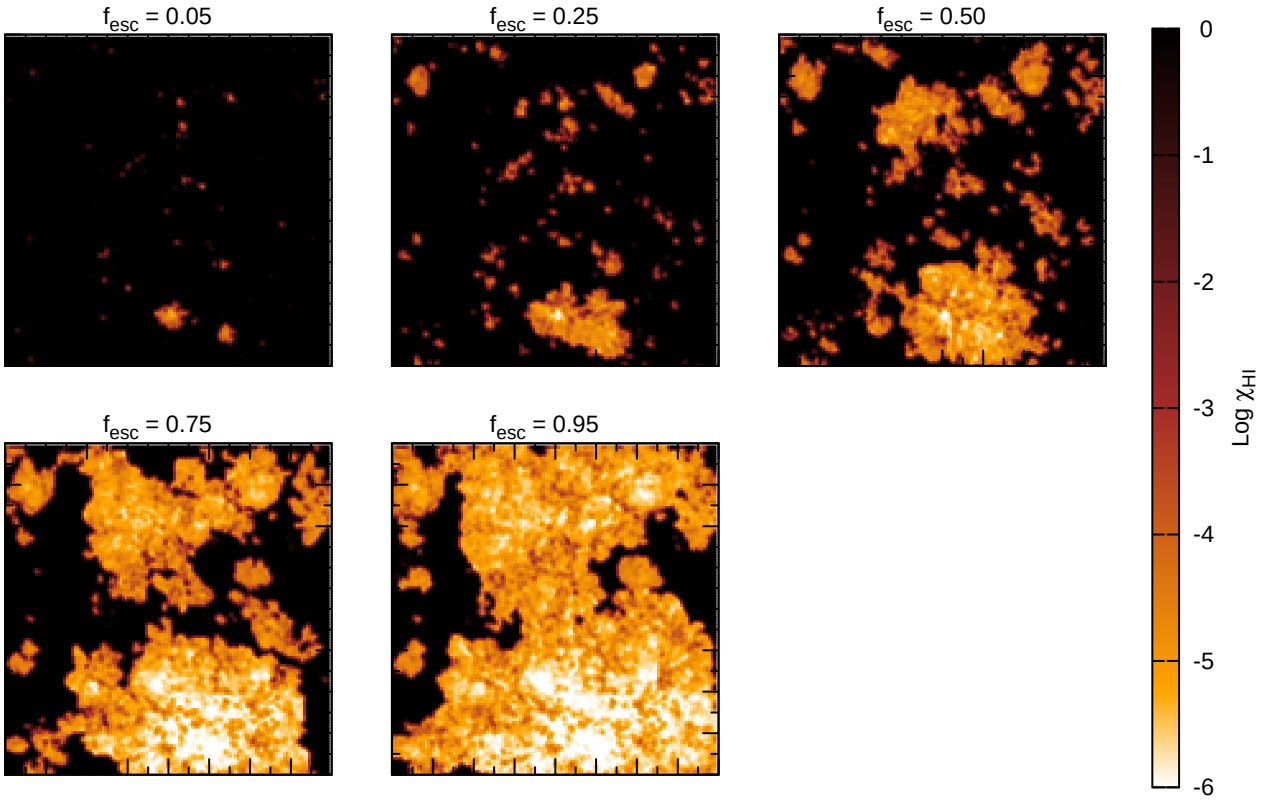

Figure 2. Maps ($80h^{-1}$ Mpc on a side) of the spatial distribution of H I in a 2D cut through the center of the simulated box at $z \simeq 6.7$ obtained by running pCRASH for 50 Myrs using the $f_{\rm esc}$ value marked above the panel. The colorbar shows the values (in log scale) of the H I fraction. As can be seen, reionization proceeds faster with increasing $f_{\rm esc}$ values.

shot of the hydrodynamical simulation as the inputs for pCRASH. For each resolved source in the SPH simulation, the luminosity and spectrum were calculated by summing up the spectra of all their star particles, as described in section 2.3; we processed 31855 resolved sources from the snapshot at $z \simeq 6.7$. The spectrum of each source was binned into 125 frequency intervals ranging from 3.21×10^{15}Hz to 3.30×10^{16}Hz. Each source emitted 10^7 rays and we used 10^6 timesteps per 500 Myrs on a 128^3 grid; we used the mean local clumping factor of each cell obtained from the underlying density distribution from the SPH simulation to account for the clumpiness of the IGM (Raičević & Theuns 2011). Depending on the escape fraction the runs were carried out on 64 or 128 processors on AIP clusters. Each simulation was run until the IGM global hydrogen fraction dropped to $\langle \chi_{HI} \rangle \lesssim 10^{-4}$, so that the entire progress of reionization could be mapped.

We now discuss the ionization fields obtained by running pCRASH on the SPH simulation snapshot at $z \simeq 6.7$ for the five different $f_{\rm esc}$ values mentioned above. Firstly, the volume of the ionized region (V_I) carved out by any source depends on its total ionizing photon output such that

$$V_I \quad \propto \quad \frac{Q f_{\rm esc}}{\chi_{HI} n_H}, \tag{2}$$

where Q is the total number of H I ionizing photons produced by the source, χ_{HI} is the H I fraction and n_H represents the number density of hydrogen atoms. From this expression, it is clear that for a given source surrounded by an IGM of a given H I density, V_I increases with $f_{\rm esc}$. In other words, given a galaxy population, at any given time, the IGM is more ionized (i.e. reionization proceeds faster) for larger $f_{\rm esc}$ values.

Secondly, the photoionization rate (Γ) at a distance r from a source depends on the source H I photon emissivity ($L_\lambda f_{\rm esc}$) such that

$$\Gamma(r) = \int_0^{\lambda_L} \frac{L_\lambda \, f_{\rm esc}}{4\pi r^2} \sigma_L \left(\frac{\lambda}{\lambda_L} \right)^3 \frac{\lambda}{hc} d\lambda, \tag{3}$$

where L_λ is the total specific ionizing luminosity of the emitter, λ_L is the Lyman limit wavelength (912 Å), σ_L is the hydrogen photoionization cross-section at $\lambda = \lambda_L$, h is the Planck constant and c represents the speed of light. Assuming ionization-recombination balance, it is this photoion-

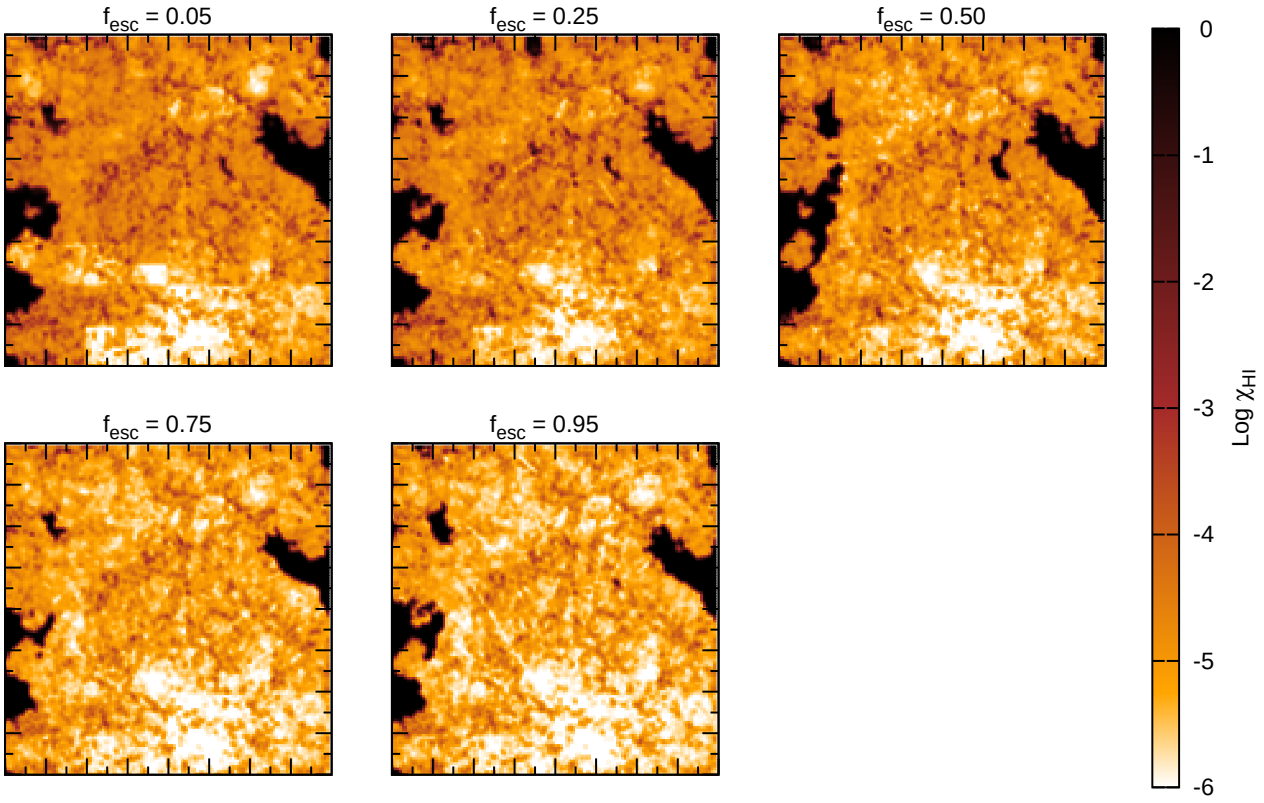

Figure 3. Maps ($80h^{-1}$ Mpc on a side) of the spatial distribution of H I in a 2D cut through the simulated box at $z \simeq 6.7$ obtained by running pCRASH using the $f_{\rm esc}$ value marked above the panel, until the average neutral hydrogen fraction drops to $\langle \chi_{HI} \rangle \simeq 0.1$. The colorbar shows the values (in log scale) of the H I fraction. As seen, while the topology of reionization looks very similar for the same average H I values, the degree of ionization close to any source increases with increasing $f_{\rm esc}$.

ization rate that determines the level of ionization, χ_{HI}, around an emitter. Hence, for a given emitter, χ_{HI} is expected to decrease for increasing values of $f_{\rm esc}$ (see also Sec. 2.4, Dayal et al. 2008).

These two effects can be clearly seen in Figs. 2 and 3: the former and latter show the ionization fields obtained for different $f_{\rm esc}$ by running pCRASH for a given time (50 Myrs) and until the IGM is ionized to a level of $\langle \chi_{HI} \rangle \simeq 0.1$, respectively. From Fig. 2, it can be clearly seen that reionization proceeds faster for increasing $f_{\rm esc}$ values: after 50 Myrs of running pCRASH, while the largest ionized region built has a size of about 15 cMpc for $f_{\rm esc} = 0.05$, the entire box is almost reionized for $f_{\rm esc} = 0.95$. Indeed, the average value of χ_{HI} drops steadily with increasing $f_{\rm esc}$ such that $\langle \chi_{HI} \rangle = (0.97, 0.82, 0.62, 0.37, 0.20)$ for $f_{\rm esc} = (0.05, 0.25, 0.5, 0.75, 0.95)$ respectively. Increasing $f_{\rm esc}$ by a factor of 19, from 0.05 to 0.95 has the effect of decreasing the neutral hydrogen fraction; while the IGM is essentially neutral for $f_{\rm esc} = 0.05$, it is almost ionized for $f_{\rm esc} = 0.95$.

From Fig. 3, we find that the topology of reionization looks similar for all the five $f_{\rm esc}$ values by the time the average H I fraction has dropped to $\langle \chi_{HI} \rangle = 0.1$. However, the time taken to reach this average ionization state is very different for the five runs; while the run with $f_{\rm esc} = 0.95$ took 80 Myrs to reach this ionization level, the runs with $f_{\rm esc} = 0.05$ took about ten times longer ($\simeq$ 800 Myrs) to build up these ionized regions. We also note that although the spatial distribution of the ionization fields looks very similar for the varying $f_{\rm esc}$ values, the level of ionization in any given cell increases with increasing $f_{\rm esc}$ as seen from the same figure (see also Eqn. 3).

To summarize, we find that increasing $f_{\rm esc}$ both accelerates the progress of reionization and leads to higher ionization fractions in the ionized regions. A combination of both these factors leads to a larger IGM Lyα transmission T_α with increasing $f_{\rm esc}$, as explained in the following.

4.2 Identifying LAEs

In this section, we start by explaining how we calculate the intrinsic Lyα luminosity produced by each simulated galaxy at $z \simeq 6.7$. We then show how we calculate the Lyα atten-

uation by ISM dust and IGM H I to determine the fraction of this intrinsic luminosity that is finally observed.

4.2.1 Intrinsic Lyα luminosity

As mentioned above, star formation in galaxies produces photons more energetic than 1 Ryd, with a certain fraction ($f_{\rm esc}$) escaping into, and ionizing the IGM. The rest of these photons ($1-f_{\rm esc}$) ionize the H I in the ISM. Due to the high density of the ISM, these electrons and protons recombine on very short timescales giving rise to a Lyα emission line of luminosity

$$L_\alpha^{int} = \frac{2}{3}Q(1-f_{\rm esc})h\nu_\alpha, \quad (4)$$

where the factor two-thirds arises due to our assumption of case-B recombinations for optically thick H I in the ISM (Osterbrock 1989), and ν_α represents the Lyα frequency in the galaxy rest frame.

However, this line is Doppler broadened by the rotation of the galaxy so that the complete line profile can be expressed as

$$L_\alpha^{int}(\nu) = \frac{2}{3}Q(1-f_{\rm esc})h\nu_\alpha \frac{1}{\sqrt{\pi}\Delta\nu_d}\exp\left[-\frac{(\nu-\nu_\alpha)^2}{\Delta\nu_d^2}\right], \quad (5)$$

where $\Delta\nu_d = (v_c/c)\nu_\alpha$. For realistic halo and disk properties, the rotation velocity of the galaxy (v_c) can range between v_h and $2v_h$, where v_h is the halo rotation velocity (Mo et al. 1998; Cole et al. 2000). We use the central value of $v_c = 1.5v_h$ in all the calculations presented in this paper.

4.2.2 Effects of dust

The intrinsic Lyα luminosity produced by a galaxy has to penetrate through dust in the ISM, with only a fraction f_α emerging out of the galactic environment. In Sec. 2.2, we have shown calculations for the total dust enrichment of each simulated galaxy and the resulting value of f_c. The relation between f_α and f_c depends on the adopted extinction curve if dust is homogeneously distributed; it also depends on the differential effects of radiative transfer on Lyα and UV photons if dust is inhomogeneously distributed/clumped (Neufeld 1991; Hansen & Oh 2006). While some pieces of evidence exist that the SN extinction curve (Bianchi & Schneider 2007) can successfully be used to interpret the observed properties of the most distant quasars (Maiolino et al. 2006) and gamma-ray bursts (Stratta et al. 2007), the effect of dust inhomogeneities in enhancing the escape fraction of Lyα photons with respect to continuum photons through the Neufeld effect (Neufeld 1991) remains controversial. On the one hand, Finkelstein et al. (2009) have found tentative observational evidence of $f_\alpha/f_c > 1$ for $z \simeq 4.5$ LAEs and Dayal et al. (2009, 2011) have shown that models require $f_\alpha/f_c > 1$ to reproduce LAE data at $z \lesssim 6$. On the other hand, Laursen et al. (2013) have shown that a value of $f_\alpha > f_c$ requires very special circumstances (no bulk outflows, very high metallicity, very high density of the warm neutral medium and a low density and highly ionized medium) that are unlikely to exist in any realistic ISM; moreover, they show that a value of $f_\alpha/f_c > 1$ results in very narrow Lyα lines that are sensitive to infalling gas, resulting in low T_α values. Due to its poor understanding, the relative escape fraction f_α/f_c is left as a free parameter in our model and its value is fixed by matching the theoretical LAE Lyα and UV LFs to the observations, as shown in Sec. 5 that follows.

4.2.3 Effects of the IGM

The Lyα photons that escape out of a galaxy unabsorbed by dust are attenuated by the H I they encounter along the line of sight (LOS) between the emitter and the observer, with a fraction $T_\alpha = e^{-\tau_\alpha}$ being transmitted through the IGM. This optical depth to H I (τ_α) can be calculated as

$$\tau_\alpha(v) = \int_{r_{em}}^{r_{obs}} \sigma_0\ \Phi\left(v + v_P\left(r\right)\right)\ n_{HI}(r)\ {\rm d}r, \quad (6)$$

where $v = (\lambda - \lambda_\alpha)\lambda_\alpha^{-1}c$ is the rest-frame velocity of a photon with frequency λ relative to the Lyα line center at $\lambda_\alpha = 1216$Å. Further, v_P accounts for the IGM peculiar velocity, $n_{HI}(r)$ the H I density at a physical distance r from the emitter, $\sigma_0 = \pi e^2 f/m_e c$ is the absorption cross section, f is the oscillator strength, e is the electron charge, m_e is the electron mass, and $\Phi(v)$ is the Voigt profile; this profile consists of a Gaussian core and Lorentzian damping wings. For regions of low H I density, pressure line broadening becomes unimportant and the line profile can be approximated by the Gaussian core. However, the Lorentzian damping wings become important in regions of high H I density and the complete profile must then be used. Although it is computationally quite expensive, we use the complete Voigt profile for all our calculations. We note that we include the effects of peculiar velocities (v_P) in determining τ_α: inflows (outflows) of gas towards (from) a galaxy will blueshift (redshift) the Lyα photons, increasing (decreasing) τ_α, which leads to a corresponding decrease (increase) in T_α. We compute τ_α by stepping through our simulation box which is divided into a grid of 128^3 cells, with each cell having a size of 117 physical kpc; this is the same grid that is used to run pCRASH, as described in Sec. 4.1. For any galaxy, we start calculating τ_α at the galaxy position $r_{em} = 0$, until the edge of the box is reached r_{obs}. The value of $v_P(r)$ and $n_{HI}(r)$ in each cell are then obtained from GADGET-2 and pCRASH runs, respectively. A single GADGET-2 snapshot at $z \simeq 6.7$ suffices for our work because the Lyα line redshifts out of resonance with H I extremely quickly; to a first approximation, the spatial scale imposed by the Gunn-Peterson damping wing on the size of the H II region corresponds to a separation of about 280 kpc (physical) at $z = 6$ (Miralda-Escude 1998). Interested readers are referred to Dayal et al. (2011) for complete details of this calculation.

We use the ionization fields obtained by running pCRASH (see Sec. 4.1) with the five different $f_{\rm esc}$ values to calculate the average T_α for each galaxy along 48 lines of sight (LOS). For a given ionization state, the final T_α value of each galaxy is taken to be the average along all 48 LOS. For each galaxy we compute the observed Lyα luminosity

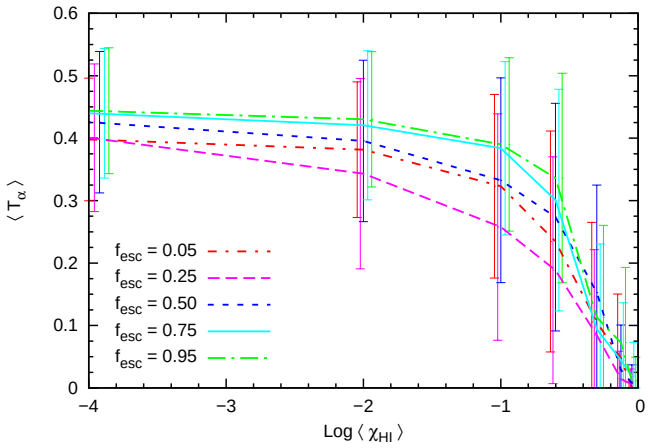

Figure 4. Mean transmission of all galaxies (averaged over 48 LOS) in the simulation snapshot at $z \simeq 6.7$ as a function of the mean IGM hydrogen neutral fraction. Red (dash-dotted), magenta (long dashed), dark blue (short dashed), light blue (dotted) and green (long dashed-dotted) lines show the relation for $f_{\rm esc} = 0.05$, 0.25, 0.5, 0.75 and 0.95 and error bars indicate the 1σ dispersion.

(L_α^{obs}) by using the individual values for f_α and T_α of the respective galaxy.

$$L_\alpha^{obs} = f_\alpha T_\alpha L_\alpha^{int}. \quad (7)$$

In consistency with current observational criteria, galaxies with $L_\alpha^{obs} \geqslant 10^{42}$erg s^{-1} and an equivalent width ($EW = L_\alpha^{obs}/L_c^{obs} \geqslant 20$Å) are then identified as LAEs and used to build the LAE UV and Lyα LFs. We note that the Lyα LFs along different LOS are subject to cosmic variance as shown in Appendix B.

We also remind the reader that T_α is fixed from the ionization state of the IGM as explained above. Then, the only free parameter that we are left with to identify LAEs is the relative escape fraction of Lyα and continuum photons i.e. f_α/f_c. This final free parameter is fixed by matching the simulated LFs to the observed ones, as explained in Sec. 5.

Before proceeding to a comparison between the theoretical results and observational data, we briefly digress to show the relation between T_α and $\langle\chi_{HI}\rangle$ for our 5 $f_{\rm esc}$ values. As can be seen from Fig. 4 (see also Sec. 4.1), the mean IGM transmission ($\langle T_\alpha\rangle$) averaged over all galaxies increases with decreasing $\langle\chi_{HI}\rangle$ values: as ionized regions grow larger, they allow all galaxies to transmit more of their Lyα flux through the IGM. The inhomogeneity of the ionized regions also leads to a huge variation in T_α as seen from the 1σ dispersions in the same figure. Finally, our mean IGM transmission values are consistent with the results obtained by Jensen et al. (2013), Iliev et al. (2008) and Dijkstra et al. (2007) for $f_{\rm esc} = 0.05$; we note that Lyα transmission calculations have not been performed for escape fractions higher than this value.

5 JOINT CONSTRAINTS ON REIONIZATION TOPOLOGY AND DUST

From Secs. 4.1 and 4.2, it is clear that $f_{\rm esc}$ affects the observed Lyα luminosity both through its effect on the intrinsic Lyα luminosity and through its effect on the ionization state of the IGM. Further, for a given $f_{\rm esc}$ and ionization state, the only free parameter left in our model is the escape fraction of Lyα photons compared to UV-continuum photons, f_α/f_c. In this section we use the LAE data accumulated by Kashikawa et al. (2011) to simultaneously constrain and find best fits to our 3 parameters, $f_{\rm esc}$, $\langle\chi_{HI}\rangle$ and f_α/f_c. We use pCRASH outputs for $\langle\chi_{HI}\rangle \simeq 0.9, 0.75, 0.5, 0.25, 0.1, 0.01$ and 10^{-4} for each of the five $f_{\rm esc} = 0.05, 0.25, 0.5, 0.75, 0.95$ at $z \simeq 6.7$. For each such combination, we start from the special case of assuming $f_\alpha/f_c = 0.68$ which corresponds to dust being homogeneously distributed in the ISM in Sec. 5.1, and progress to the more general scenario of varying f_α/f_c to best fit the observations, in Sec. 5.2.

5.1 A special case: homogeneous dust

As shown in Eqn. 4, the intrinsic Lyα luminosity produced by a galaxy depends on the fraction of H I ionizing photons that ionize the H I in the ISM. It is thus naturally expected that L_α^{int} decreases with increasing $f_{\rm esc}$ since this leads to fewer photons being available for ionization in the ISM. This behaviour can be seen from panel (a) of Fig. 5 where we find that the amplitude of the Lyα LF drops by a factor of about 40 as $f_{\rm esc}$ increases from 0.05 to 0.95. This drop seems surprising at the first glance: as $f_{\rm esc}$ increases by a factor of about 19, the intrinsic Lyα LF would be expected to drop by the same amount. However, this result can be easily explained by the fact that we identify galaxies as LAEs based on the Lyα luminosity being larger than 10^{42}erg s^{-1} and an $EW \geqslant 20$Å. As $f_{\rm esc}$ increases, fewer and fewer galaxies are able to fulfil these selection criteria, leading to an enhanced drop in the amplitude of the Lyα LF.

The ratio f_α/f_c depends on many physical effects (see e.g. Laursen et al. 2013), including the distribution of the Lyα sources in the dusty ISM (Scarlata et al. 2009), the ISM H I column densities and velocities. However, a natural consequence of simulating cosmological volumes is that we are unable to resolve the ISM of individual galaxies. We therefore start with the special scenario wherein dust is homogeneously distributed in the ISM and Lyα photons are not scattered by dust and H I within the ISM. Since SNII are assumed to be the main sources of dust in our model, we deduce the ratio $f_\alpha/f_c = 0.68$ purely from the corresponding SN extinction curve (Bianchi & Schneider 2007). This fixed ratio is then applied uniformly to all galaxies in the simulation snapshot at $z \simeq 6.7$. Once f_α has been fixed using this ratio, the only two parameters that can affect the slope and amplitude of the Lyα LFs are $f_{\rm esc}$ and χ_{HI}.

We start by discussing the Lyα LF evolution as a function of $\langle\chi_{HI}\rangle$. As expected from Eqn. 6, for a given $f_{\rm esc}$, τ_α decreases with decreasing $\langle\chi_{HI}\rangle$, leading to an increase in the IGM Lyα transmission. This naturally results in an increase in the amplitude of the Lyα LF by making galax-

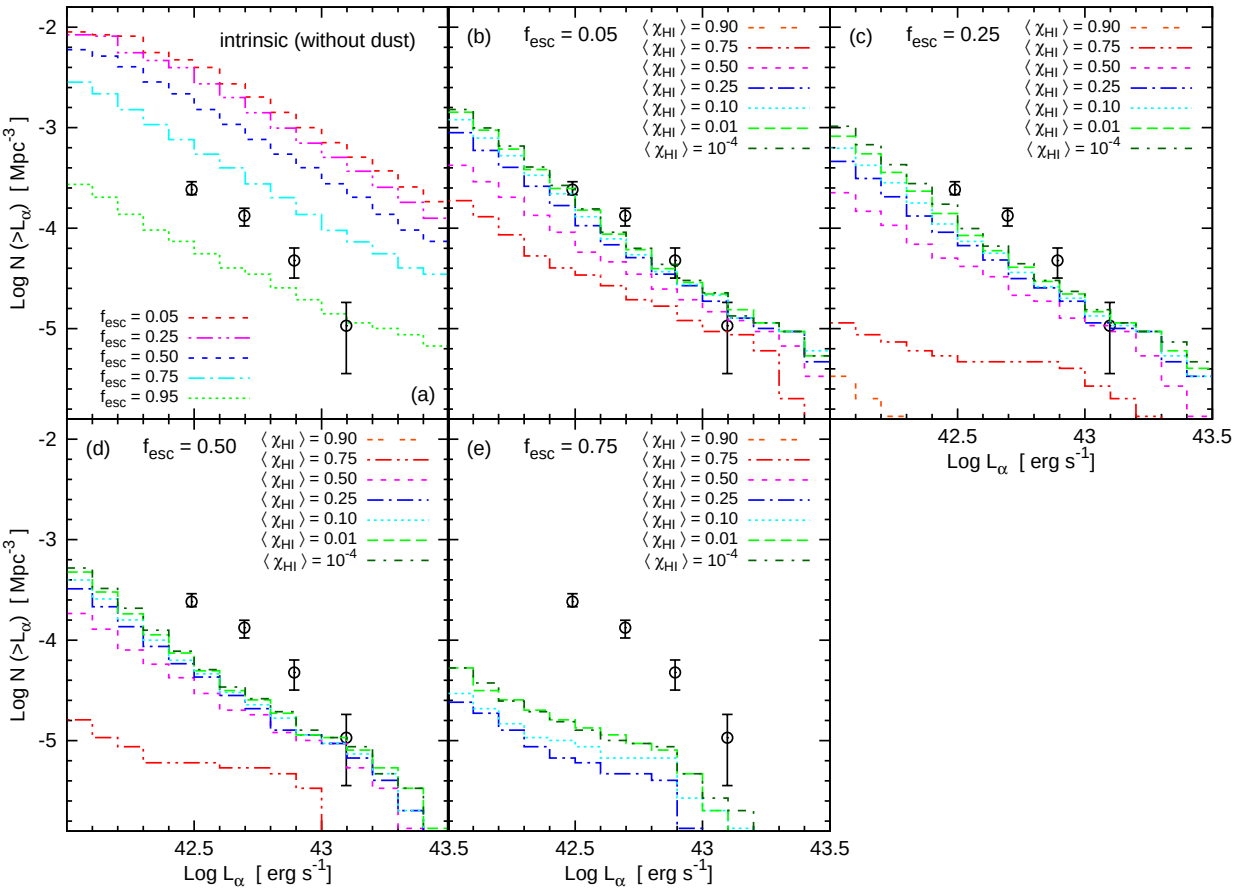

Figure 5. The cumulative Lyα LFs. Panel (a) shows the intrinsic Lyα LFs for escape fractions $f_{\rm esc} = 0.05$, 0.25, 0.50, 0.75, as marked. The lines in the other panels show the results for homogeneously distributed SNII dust ($f_\alpha/f_c = 0.68$) for different $\langle\chi_{HI}\rangle$ states ($\langle\chi_{HI}\rangle \simeq 0.90$, 0.75, 0.50, 0.25, 0.10, 0.01, 10^{-4}) obtained using the fixed $f_{\rm esc}$ value marked above the panel. In each panel, black open circles show the Lyα LFs at $z \simeq 6.5$ inferred observationally by Kashikawa et al. (2011). Due to the EW selection criterion no LAEs are identified for $f_{\rm esc} = 0.95$.

ies more luminous in the observed Lyα luminosity, L_α^{obs}, as can be seen from panels (b)-(e) of Fig. 5. However, the effect of decreasing χ_{HI} is the strongest on the visibility of the faintest galaxies and decreases with increasing luminosity. This is because the spatial scale imposed by the Gunn-Peterson damping wing on the size of the H II region corresponds to a separation of about 280 kpc (physical) at $z \simeq 7$ (Miralda-Escude 1998). The most massive galaxies are easily able to carve out H II regions of this size as a result of their relatively large H I ionizing photon output. However, in the initial stages of reionization, only those faint galaxies that are clustered are able to build H II regions of this size and become visible as LAEs (McQuinn et al. 2007a; Dayal et al. 2009). Hence, for a given $f_{\rm esc}$, the faint-end slope of the Lyα LF becomes steeper with decreasing $\langle\chi_{HI}\rangle$ values as seen from panels (b)-(e) of Fig. 5. We also see that the slope and amplitude of the Lyα LFs start converging for $\langle\chi_{HI}\rangle \simeq 10^{-2}$; this corresponds to the average H I fraction at which galaxies typically inhabit H II regions such that the red part of the Lyα line escapes unattenuated by H I .

We now discuss the evolution of the Lyα LFs with $f_{\rm esc}$. As we have already noted in Fig. 3, although the spatial distribution of the ionization fields looks very similar for the varying $f_{\rm esc}$ values for a given $\langle\chi_{HI}\rangle$, the χ_{HI} value in any given cell decreases with increasing $f_{\rm esc}$. This leads to an increase in T_α with $f_{\rm esc}$ such that for $\langle\chi_{HI}\rangle \simeq 0.1$, averaged over all LAEs, $\langle T_\alpha\rangle = (0.43, 0.45, 0.48, 0.59)$ for $f_{\rm esc} = (0.05, 0.25, 0.50, 0.75)$. However, this slight increase in T_α is compensated by the decrease in the intrinsic Lyα luminosity with increasing $f_{\rm esc}$ as shown in panel (a) of Fig. 5. As a result, the amplitude of the resulting Lyα LFs decreases slightly as $f_{\rm esc}$ increases from 0.05 to 0.5 for a given $\langle\chi_{HI}\rangle$; however, the slopes are very similar since $f_{\rm esc}$ affects the intrinsic luminosity of all simulated galaxies by the same factor. The Lyα LF drops steeply between $f_{\rm esc} = 0.5$ and 0.75 and there are no simulated galaxies that would be identified as LAEs for $f_{\rm esc} = 0.95$. This steep drop for

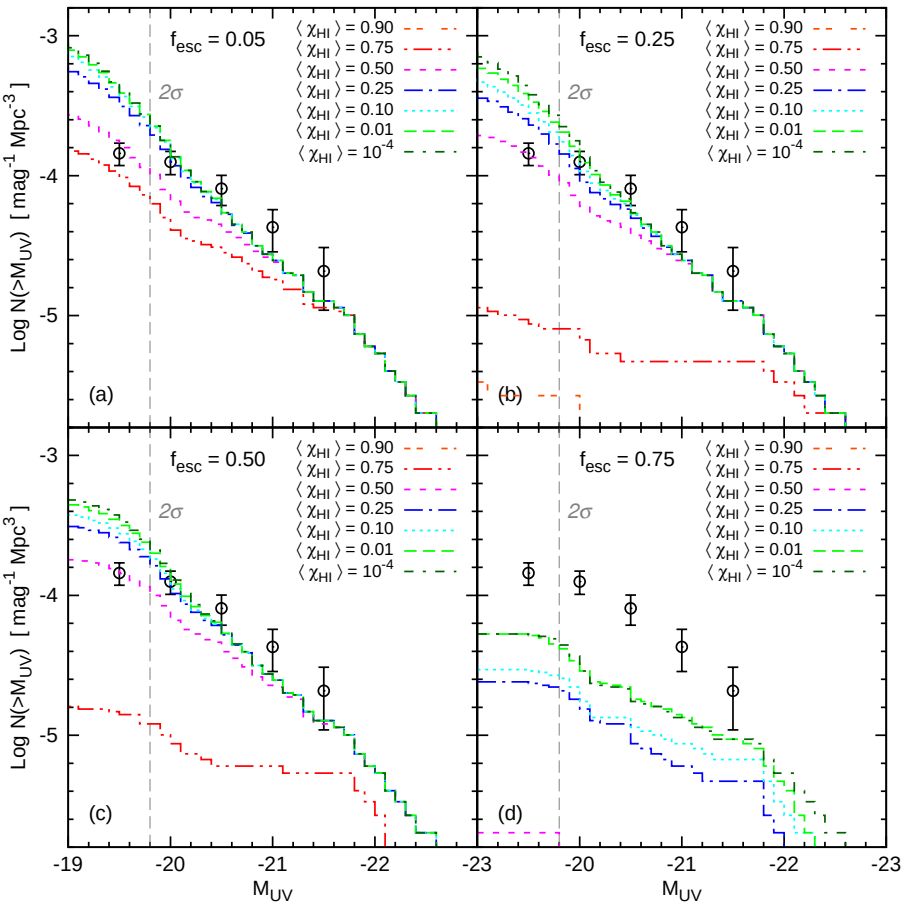

Figure 6. The cumulative UV LFs for simulated LAEs using a homogeneous dust case ($f_\alpha/f_c = 0.68$). The lines in the panels show the UV LFs for different $\langle\chi_{HI}\rangle$ states ($\langle\chi_{HI}\rangle \simeq 0.90, 0.75, 0.50, 0.25, 0.10, 0.01, 10^{-4}$) obtained using the fixed $f_{\rm esc}$ value marked above the panel. In each panel, black open circles show the LAE UV LFs at $z \simeq 6.5$ inferred observationally by Kashikawa et al. (2011). The vertical grey dotted lines indicate the limiting 2σ magnitude in the z' band (see Kashikawa et al. 2011); measurements for fainter magnitudes may be uncertain because the corresponding z'-band magnitudes are no longer reliable. Due to the EW selection criterion no LAEs are identified for $f_{\rm esc} = 0.95$.

$f_{\rm esc} > 0.5$ arises due to our imposed criterion of the observed Lyα EW being larger than 20Å. For a continually star-forming galaxy with an age of about 200Myr, a stellar metallicity of $Z_* = 0.02Z_\odot$ and $f_{\rm esc} = 0$, the intrinsic Lyα EW has a value of about 114Å; we note that this intrinsic EW would decrease for increasing values of Z_* and $f_{\rm esc}$. For a value of $f_{\rm esc} = (0.75,\ 0.95)$, this intrinsic EW then reduces to about (28.5, 5.7)Å . Then, taking into account the effect of the IGM transmission very few (none) of our simulated galaxies fulfil the EW selection criterion for $f_{\rm esc} = 0.75$ (0.95) leading to a steep drop in the number density of LAEs; the total number density of LAEs drops to zero for $f_{\rm esc} = 0.95$.

Finally, we note that both the slope and amplitude of the simulated Lyα LFs are in agreement with observations for $f_{\rm esc} = 0.05$ and $\langle\chi_{HI}\rangle \leqslant 0.1$; for $f_{\rm esc} \geqslant 0.25$, the simulated Ly$\alpha$ LFs are underestimated with respect to the data, even for a fully ionized IGM.

The UV LFs are not directly dependent on the IGM ionization state. However, both their slope and amplitude are affected by $\langle\chi_{HI}\rangle$ since these are the UV LFs for the simulated galaxies that would be identified as LAEs on the basis of L_α^{obs} and the EW. It is interesting to note that with our deeper Lyα luminosity limit of $L_\alpha^{obs} \geqslant 10^{42}$erg s^{-1}compared to the observational limit of $10^{42.4}$ erg s^{-1}, we find that the cumulative UV LFs keep rising until $M_{UV} \leqslant -19$ for $f_{\rm esc} \leqslant 0.5$ as seen from panels (a)-(c) of Fig. 6. From these same panels, we find that the bright-end slope of the UV LF ($M_{UV} \leqslant -21.5$) matches the observed UV LFs for all values of $\langle\chi_{HI}\rangle$ and $f_{\rm esc} \leqslant 0.5$. Further, the UV LFs start converging at much higher values of $\langle\chi_{HI}\rangle \simeq 0.25$, compared to the value of 0.1 required for the Lyα LFs to settle. Similar to the behaviour seen for the Lyα LF, for a given $f_{\rm esc} \leqslant 0.5$,

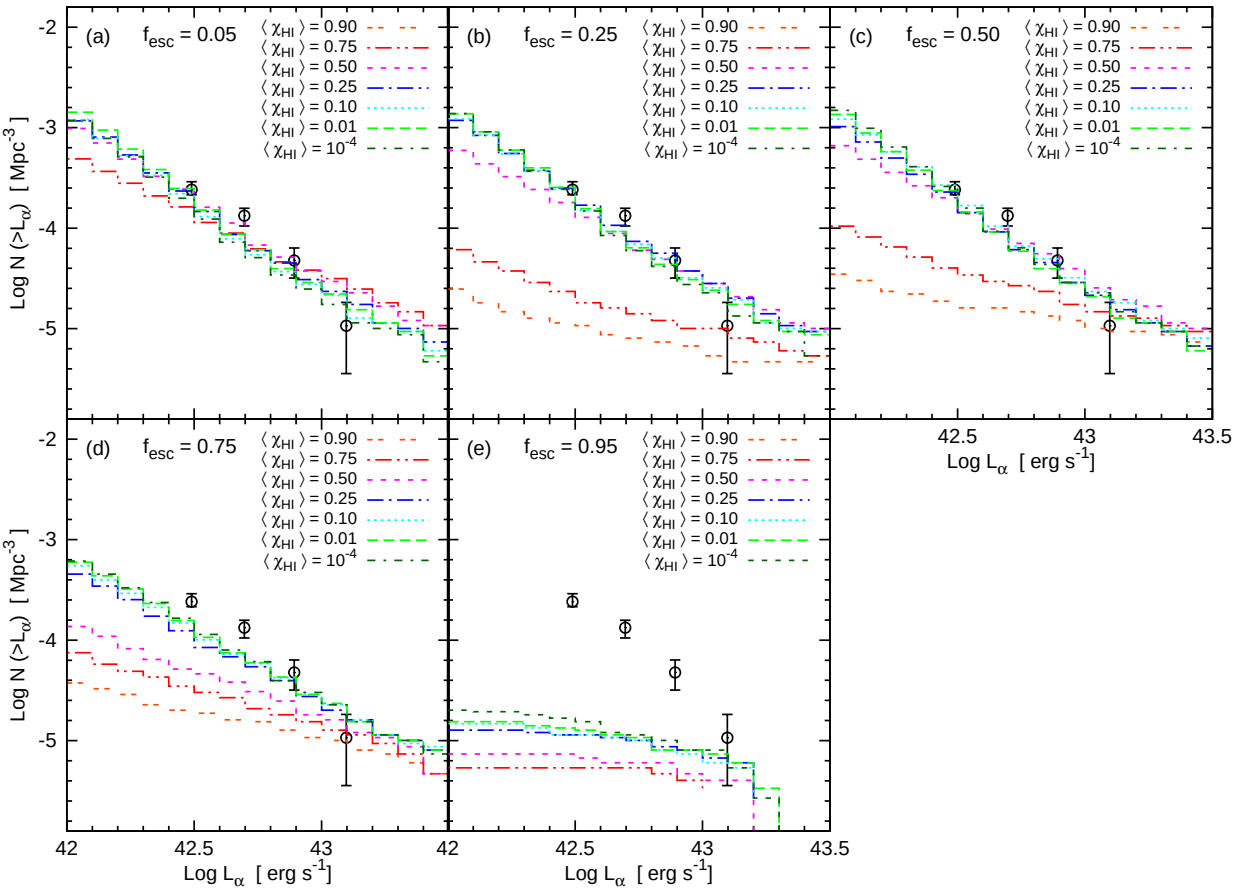

Figure 7. The cumulative Lyα LFs. The panels show the best-fit simulated results for the f_α/f_c values shown in Table 1. The panels show the results for different $\langle\chi_{HI}\rangle$ states ($\langle\chi_{HI}\rangle \simeq 0.90$, 0.75, 0.50, 0.25, 0.10, 0.01, 10^{-4}) obtained using the fixed $f_{\rm esc}$ value marked above the panel. In each panel, black open circles show the Lyα LFs at $z \simeq 6.5$ inferred observationally by Kashikawa et al. (2011).

the faint end of the UV LF steepens with decreasing $\langle\chi_{HI}\rangle$ as more and more of these galaxies are able to transmit enough of their Lyα flux to be visible as LAEs. Again, for a given $\langle\chi_{HI}\rangle$, while the amplitude of the UV LFs decreases slightly between $f_{\rm esc} = 0.05$ and 0.5, the slope remains the same. The steep drop in the number of LAEs for $f_{\rm esc} \simeq 0.75$ naturally leads to a drop in the UV LF shown in panel (d) of the same figure; as for the Lyα LF, the UV LF amplitude is zero for $f_{\rm esc} = 0.95$ due to no simulated galaxies being classified as LAEs.

Finally, we note that by jointly reproducing the observed Lyα and UV LFs, we can constrain for $f_{\rm esc} = 0.05$ one of the most important parameters for reionization: $\langle\chi_{HI}\rangle \leqslant 0.1$ or $\langle T_\alpha\rangle_{LAE} \geqslant 0.43$.

However, we caution the reader that this result is only valid in case the ISM dust is homogeneously distributed. Since using only the UV LFs allows a much larger parameter range of $\langle\chi_{HI}\rangle \leqslant 0.25$, a question that arises is whether this larger parameter space could also be reconciled with the Lyα LFs given clumped dust that could increase L_α^{obs} by increasing f_α. We carry out these calculations in Sec. 5.2 that follows.

5.2 Clumped dust

A number of works have shown that inhomogeneously distributed (clumped) dust in the ISM can enhance the escape fraction of Lyα photons compared to UV photons which are not resonantly scattered by H I (Neufeld 1991; Hansen & Oh 2006). However, the amount by which the ratio f_α/f_c can be enhanced by clumped dust sensitively depends on the amount of dust that is bound in cold neutral gas clouds, and the number of these encountered by Lyα photons within the galaxy. Since such sub-grid parameters can not be resolved by our cosmological simulation, we use f_α/f_c as a free parameter and explore the range required to reproduce the data for the different $f_{\rm esc}$ and $\langle\chi_{HI}\rangle$ combinations discussed in Sec. 5.1.

As shown in Section 5.1, an increasing $f_{\rm esc}$ reduces the intrinsic Lyα luminosity for all galaxies, leading to a drop in the amplitude of the Lyα LF. However, since $L_\alpha^{obs} \propto (1-$

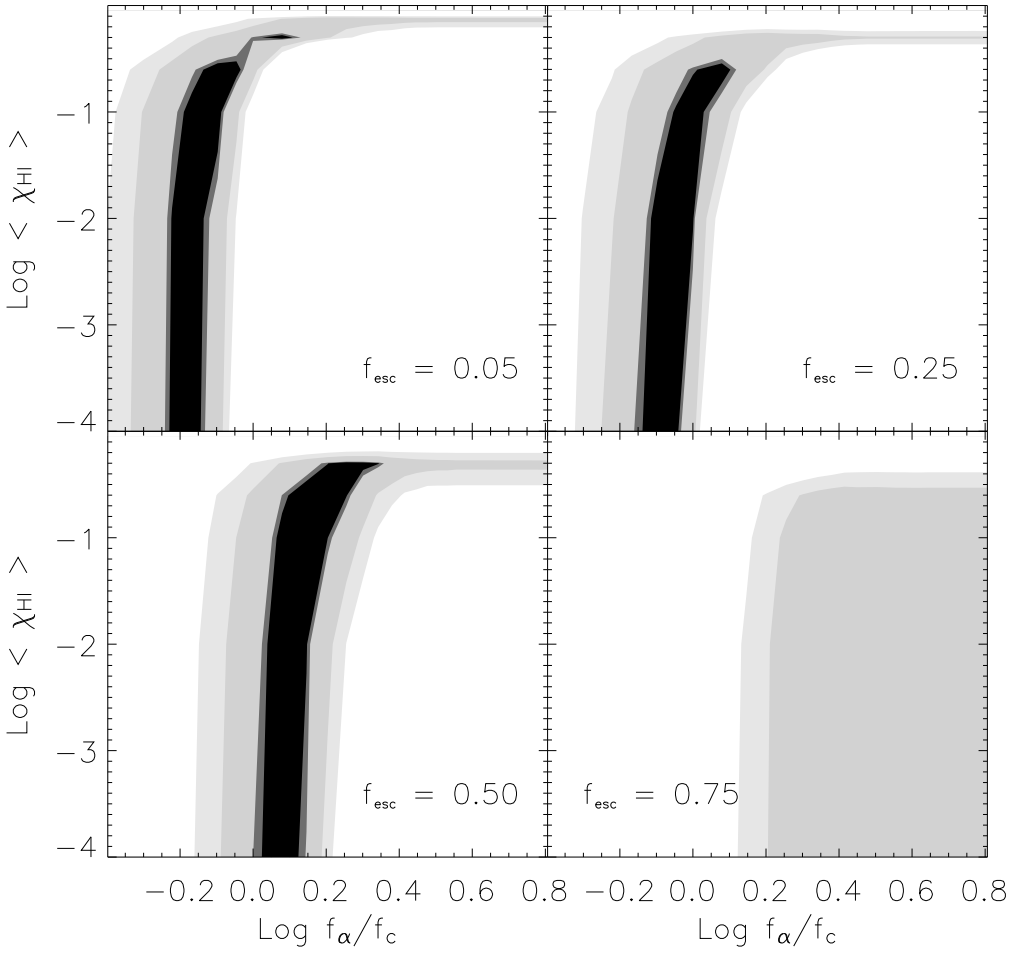

Figure 8. $1-5\sigma$ probability contours (black to light gray respectively) for the combinations of $\langle\chi_{HI}\rangle$, $f_{\rm esc}$ and f_α/f_c shown in Table. 1 that best fit the observed Lyα LF data at $z\simeq 6.5$ Kashikawa et al. (2011). Within a 1σ error, we can not distinguish between $\langle\chi_{HI}\rangle \simeq 10^{-4}$ to 0.5, f_α/f_c from 0.6 to 1.8 and $f_{\rm esc}$ ranging between 0.05 and 0.5. There exists a *degeneracy* between the IGM ionization state, escape fraction of H I ionizing photons and the dust clumping inside high-redshift galaxies such that a decrease in the IGM Lyα transmission can be compensated by an increase in the intrinsic Lyα luminosity produced, and the fraction of this luminosity that can escape the galaxy.

$f_{\rm esc})f_\alpha T_\alpha$, a decrease in the intrinsic Lyα luminosity (due to an increasing $f_{\rm esc}$) can be compensated by a larger fraction of Lyα photons escaping out of the galaxy (i.e. a higher f_α) and/or a larger amount being transmitted through the IGM (i.e. a larger T_α). Hence, for a given $\langle\chi_{HI}\rangle$ (i.e. T_α) by allowing values of $f_\alpha/f_c > 0.68$, the amplitude of the Lyα LF can be boosted. However, it is important to note that since we use a constant value of f_α/f_c for all galaxies, it only changes the amplitude of the Lyα LF at the bright end; raising this ratio makes the faint-end slope slightly steeper since a number of galaxies which are at our detection limit ($L_\alpha \geqslant 10^{42}$erg s^{-1}and $EW \geqslant 20$Å) become visible as LAEs with increasing f_α/f_c.

It is interesting to note that even using f_α/f_c ratios such that f_α saturates to 1, the simulated Lyα LFs are well below the observations for $\langle\chi_{HI}\rangle \simeq 0.75$, for all $f_{\rm esc} = 0.05$ to 0.95, as seen from panels (a)-(e) of Fig. 7. This is because the H II regions built by faint galaxies are too small to allow a large IGM Lyα transmission, even for $f_{\rm esc} = 0.95$. We now discuss the results for varying $f_{\rm esc}$: as mentioned in Sec. 5.1, the Lyα and UV LFs can be well reproduced using the homogeneous dust case for $f_{\rm esc} = 0.05$ for $\langle\chi_{HI}\rangle \leqslant 0.1$. In the case of clumped dust, the simulated LFs match the observations for $f_{\rm esc} = 0.05$ for $\langle\chi_{HI}\rangle$ as high as 0.5, provided that the decrease in T_α is compensated by f_α/f_c increasing to 1.2 (see table 1). For $f_{\rm esc} = 0.25, 0.5$, within a 1σ error the simulated LFs can be reconciled with the observations for $\langle\chi_{HI}\rangle \leqslant 0.5$, given that f_α/f_c increases to 1.6, 1.8, respectively as shown in table 1; however, due to a decrease in the intrinsic Lyα luminosity and EW, the faint-end slope of the simulated LFs is always under-estimated with respect to the data for $\langle\chi_{HI}\rangle \geqslant 0.5$. As $f_{\rm esc}$ increases to 0.75 and above, the amplitude of the Lyα LFs can not be boosted up to the observed value, even for $f_\alpha = 1$; although the H II regions

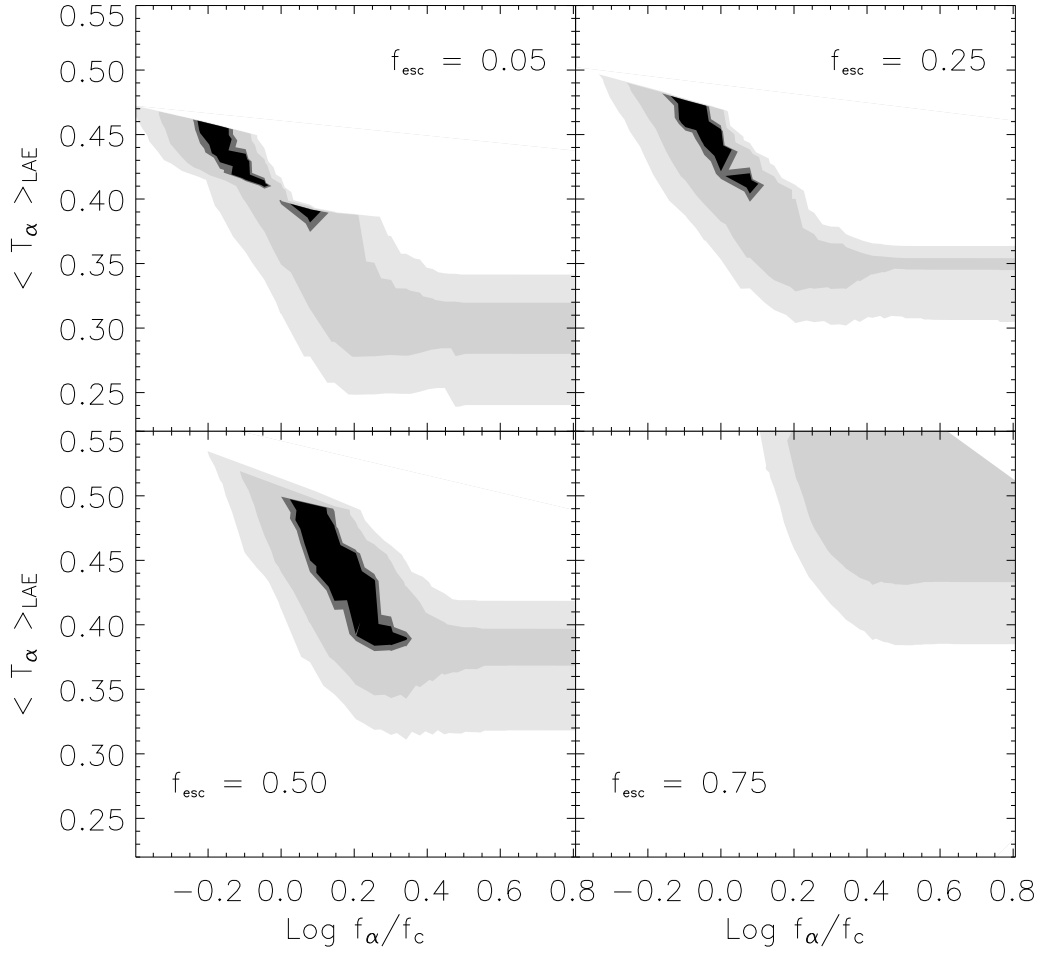

Figure 9. $1-5\sigma$ probability contours (black to light gray respectively) for the combinations of $\langle\chi_{HI}\rangle$, $f_{\rm esc}$ and f_α/f_c shown in Table. 1 that best fit the observed Lyα LF data at $z\simeq 6.5$ Kashikawa et al. (2011). Within a 1σ error, we can not distinguish between $\langle T_\alpha\rangle_{LAE}\simeq 0.38$ to 0.5, f_α/f_c from 0.6 to 1.8 and $f_{\rm esc}$ ranging between 0.05 and 0.5. There exists a *degeneracy* between the IGM Lyα transmission, escape fraction of H I ionizing photons and the dust clumping inside high-redshift galaxies such that a decrease in the IGM Lyα transmission can be compensated by an increase in the intrinsic Lyα luminosity produced, and the fraction of this luminosity that can escape the galaxy.

built by these galaxies are very large as a result of the large H I ionizing photon escape fraction leading to large T_α values, the EW of the Lyα line prevents most of these galaxies from being classified as LAEs (see also Sec. 5.1 above).

We therefore find a *three-dimensional degeneracy* between the IGM ionization state $\langle\chi_{HI}\rangle$, the escape fraction of H I ionizing photons ($f_{\rm esc}$) and the clumped/inhomogeneous distribution of dust in the ISM of galaxies (governing f_α/f_c) such that a decrease in L_α^{int} with increasing $f_{\rm esc}$ can be compensated by a larger T_α and f_α/f_c. However, we find that the $\langle\chi_{HI}\rangle$ values which reproduce the observations decrease with increasing $f_{\rm esc}$ because an increasing f_α can not compensate for the decrease in the intrinsic Lyα luminosity. This degeneracy can be seen from Fig. 8 where we show contours of $1-5\sigma$ deviations from the observations (Kashikawa et al. 2011), obtained by computing the χ^2 values for all the combinations of $f_{\rm esc}=(0.05,..,0.95)$, $\langle\chi_{HI}\rangle=(10^{-4},..,0.90)$ and $f_\alpha/f_c=(0.60,..,1.8)$, as shown in Table. 1.

The relation between $\langle\chi_{HI}\rangle$ and $\langle T_\alpha\rangle$ is complex due to the dependency upon the reionization topology as shown in Dijkstra et al. (2011) (see also Fig. 4 and Jensen et al. 2013) and the assumed line shape (e.g. Gaussian, double-peaked, Jensen et al. 2013; Laursen et al. 2011; Duval et al. 2014). For this reason we also show the three-dimensional degeneracy in terms of the mean transmission across all LAEs ($\langle T_\alpha\rangle_{LAE}$) for a given combination of $f_{\rm esc}$ and f_α/f_c in Fig. 9.

We note that for a given $\langle\chi_{HI}\rangle$ the mean transmission of all LAEs $\langle T_\alpha\rangle_{LAE}$ decreases for increasing f_α/f_c: with rising f_α/f_c more galaxies, with lower values of T_α, are identified as LAEs, leading to a decline in $\langle T_\alpha\rangle_{LAE}$. This effect can be seen for the maximum $\langle T_\alpha\rangle_{LAE}$ values, within a 4σ error, in

Table 1. For the $\langle\chi_{HI}\rangle$ value shown in column 1, for the $f_{\rm esc}$ value shown as a subscript in each of the columns 2-4, we show the f_α/f_c ratio required to fit the simulated LAE Lyα and UV LFs to those observed by Kashikawa et al. (2011) within a $1-\sigma$ error. Dashes indicate that the simulated LFs could not be matched to the observations within a $1-\sigma$ error, even for the maximum possible value of $f_\alpha = 1$.

$\langle\chi_{HI}\rangle$	$(f_\alpha/f_c)_{0.05}$	$(f_\alpha/f_c)_{0.25}$	$(f_\alpha/f_c)_{0.5}$
0.50	1.2	1.6	1.8
0.25	0.8	1.2	1.4
0.10	0.68	1.0	1.4
0.01	0.68	0.9	1.2
10^{-4}	0.60	0.8	1.2

each panel of Figure 9 and it demonstrates the dependency of $\langle T_\alpha\rangle_{LAE}$ on f_α/f_c.

From Figure 8 and 9, we see that within a 1σ error, the observed Lyα and UV LFs can be reproduced for $f_{\rm esc}$ values ranging between $0.05-0.5$ and $\langle\chi_{HI}\rangle \simeq 10^{-4}-0.5$ or $\langle T_\alpha\rangle \simeq 0.38-0.5$, provided that the decreasing intrinsic Lyα luminosity (with increasing $f_{\rm esc}$) and decreasing IGM transmission (with increasing $\langle\chi_{HI}\rangle$) is compensated by an increasing $f_\alpha/f_c = 0.6$ to 1.8. This implies that if dust is indeed clumped in the ISM of high-redshift galaxies such that the relative Lyα escape fraction can be as high as 1.8 times the UV escape fraction, we can not differentiate between a universe which is either completely ionized or half neutral (or where $38-50\%$ of LAE Lyα radiation is transmitted through the IGM) or an $f_{\rm esc}$ ranging between 5-50%. This parameter space is much larger than that allowed for a homogeneous dust distribution, where matching to the observations requires $f_{\rm esc} = 0.05$ and $\langle\chi_{HI}\rangle \leqslant 0.1$ ($\langle T_\alpha\rangle_{LAE} \geqslant 0.43$).

6 CONCLUSIONS

In this work we couple state of the art cosmological simulations run using GADGET-2 with a dust model and a radiative transfer code (pCRASH) to build a physical model of $z \simeq 6.7$ LAEs to simultaneously constrain the IGM reionization state, the escape fraction of H I ionizing photons and ISM dust distribution (homogeneous/clumped).

We start by validating the properties of the simulated galaxy population against observations of high-redshift ($z \simeq 6-8$) LBGs. Identifying bound structures using the Amiga Halo Finder, simulated galaxies which are complete in the halo mass function ($M_h \geqslant 10^{9.2} M_\odot$), contain a minimum of $4N$ gas particles ($N = 40$) and a minimum of 10 star particles are identified as the "resolved" population". For each such resolved galaxy, we use the mass, age and metallicity of each of its star particles to build the composite spectra. We use a dust model (Dayal et al. 2010) that calculates the SNII dust-enrichment depending on the entire star formation history of a given galaxy, to obtain the associated escape fraction of UV photons. Once these calculations are carried out, galaxies with a dust-attenuated UV magnitude $M_{UV} \leqslant -17$ are identified as LBGs at $z \simeq 6-8$. Comparing the predictions by the simulation against LBG observations, we find that the slope and amplitude of the dust-attenuated UV LFs are in good agreement with the data at $z \simeq 6, 7$ while the UV LF at $z \simeq 8$ requires no dust to match to the observations, such that $f_c \simeq (0.5, 0.6, 1.0)$ at $z \simeq (6, 7, 8)$, averaged over all LBGs. The theoretical Schechter parameters are found to be $\alpha = (-1.9 \pm 0.2, -2.0 \pm 0.2, -1.8 \pm 0.2)$ and $M_{UV,*} = (-19.8 \pm 0.3, -19.7 \pm 0.2, -19.9 \pm 0.3)$ at $z \simeq (6, 7, 8)$, and are consistent with those inferred observationally (McLure et al. 2009, 2013; Bouwens et al. 2011). We also find that the theoretical LBG stellar mass functions, SMDs and sSFRs are in excellent agreement with the data at $z \simeq 6-8$ (see Appendix A).

Once that the physical properties and dust enrichment of the simulated galaxy population have been validated against the mentioned observational data sets, we proceed to modelling LAEs. This requires further information on (a) the fraction of the H I ionizing photons produced by a galaxy that are absorbed by ISM H I ($1 - f_{\rm esc}$) and contribute to the Lyα emission line; the rest ($f_{\rm esc}$) emerge out and contribute to reionization, (b) the relative effect of ISM dust on Lyα and UV photons (f_α/f_c), and (c) the level to which the IGM is ionized by the galaxy population ($\langle\chi_{HI}\rangle$), in order to calculate the IGM Lyα transmission. Since $f_{\rm esc}$ remains poorly constrained with proposed values ranging between 1-100% (e.g. Ricotti & Shull 2000; Gnedin et al. 2008; Ferrara & Loeb 2013), we use five different values of $f_{\rm esc} = 0.05, 0.25, 0.5, 0.75, 0.95$ to run the radiative transfer code (pCRASH) in order to obtain various "reionization" states of the simulated volume as it evolves from being fully neutral ($\langle\chi_{HI}\rangle \simeq 1$) to completely ionized ($\langle\chi_{HI}\rangle \simeq 10^{-4}$); pCRASH follows the time evolution of the ionization fractions (H I and He II , He III) and temperature given the spectra of the source galaxy population. Once these calculations are carried out, galaxies with $L_\alpha^{obs} \geqslant 10^{42}$erg s^{-1} and $EW \geqslant 20$Å are identified as LAEs; the only free parameter of the model (f_α/f_c) is then fixed by matching the simulated LFs to the observations.

We start from the simplest case of considering the SNII produced dust to be *homogeneously distributed* in the ISM. The SNII extinction curve yields $f_\alpha/f_c = 0.68$. Using this model, we find that for a given $f_{\rm esc}$, the IGM Lyα transmission increases with decreasing $\langle\chi_{HI}\rangle$, with this increase being most important for the smallest galaxies; as $\langle\chi_{HI}\rangle$ decreases, even small galaxies are able to ionize a large enough H II region around themselves to be visible as LAEs. Hence, the Lyα LF becomes *steeper* with decreasing $\langle\chi_{HI}\rangle$ for any given $f_{\rm esc}$ value. Further, for a given $\langle\chi_{HI}\rangle$, although the ionization fields look very similar for different $f_{\rm esc}$ values, the degree of ionization (χ_{HI}) in any cell increases with $f_{\rm esc}$ due to an increase in the H I ionizing photon emissivity. This leads to a slight increase in T_α with $f_{\rm esc}$ for a given $\langle\chi_{HI}\rangle$. However, this increase is more than compensated by the decrease in the intrinsic Lyα luminosity with increasing $f_{\rm esc}$ (as less photons are available for ionizations in the ISM), as a result of which the Lyα LF decreases slightly in amplitude with $f_{\rm esc}$ for a given $\langle\chi_{HI}\rangle$. Finally, comparing simulated Lyα and UV LFs with observations, we find that for a ho-

mogeneous ISM dust distribution and $f_{\rm esc} = 0.05$, we can *constrain* $\langle\chi_{HI}\rangle \leqslant 0.1$ *or* $\langle T_\alpha\rangle_{LAE} \geqslant 0.43$.

We also explore the scenario of dust being inhomogeneously distributed/clumped in the ISM of high-redshift galaxies, boosting up the ratio of f_α/f_c. For a given $\langle\chi_{HI}\rangle$ value, an increase in $f_{\rm esc}$ leads to a drop in the amplitude of the Lyα LF due to a decrease in L_α^{int}, as mentioned above. In the clumped dust scenario, this decrease can be compensated by an increase in f_α. For $\langle\chi_{HI}\rangle \simeq 0.5$, $f_{\rm esc}$ values as high as 0.5 can be reconciled with the data, given that f_α/f_c increases from $\simeq 0.6$ to 1.8 as $f_{\rm esc}$ increases from 0.05 to 0.5. We thus find a *three-dimensional degeneracy* between $\langle\chi_{HI}\rangle$, $f_{\rm esc}$ and f_α/f_c such that a decrease in L_α^{int} with increasing $f_{\rm esc}$ can be compensated by a larger T_α and f_α/f_c. Due to the model dependency (e.g. Lyα line profile, reionization topology) of the $\langle\chi_{HI}\rangle$ -$\langle T_\alpha\rangle$ relation we also rephrase our result by converting the $\langle\chi_{HI}\rangle$ values to the corresponding mean transmission values for LAEs ($\langle T_\alpha\rangle_{LAE}$). Within an 1σ error, we find that allowing for clumped dust, the data can be reproduced for a wide parameter space of $\langle T_\alpha\rangle_{LAE} \simeq 0.38 - 0.50$ or $\langle\chi_{HI}\rangle \simeq 0.5 - 10^{-4}$, $f_{\rm esc} \simeq 0.05 - 0.5$ and $f_\alpha/f_c \simeq 0.6 - 1.8$, i.e., if dust is indeed clumped in the ISM of high-redshift galaxies such that the relative Lyα escape fraction can be as high as 1.8 times the UV escape fraction, we can not differentiate between a universe which is either completely ionized or half neutral or where on average $38-50\%$ of the Lyα radiation is transmitted, or has an $f_{\rm esc}$ ranging between 5-50%. We caution the reader that although the constraints in terms of $\langle T_\alpha\rangle_{LAE}$ account for the model dependent relation between $\langle\chi_{HI}\rangle$ and $\langle T_\alpha\rangle$, the value of $\langle T_\alpha\rangle_{LAE}$ sensitively depends on the galaxies that are classified as LAEs for a given combination of $f_{\rm esc}$, $\langle\chi_{HI}\rangle$ and f_α/f_c.

We now discuss some of the caveats involved in this work. Firstly, an enhancement of the escape fraction of Lyα photons with respect to continuum photons via the Neufeld effect (Neufeld 1991) in a clumpy ISM remains controversial: on the one hand Hansen & Oh (2006) showed that such enhancement was possible if the Lyα photons encountered a certain number of "clumps". On the other hand, Laursen et al. (2013) have shown that enhancing the ISM Lyα escape fraction requires very specific conditions (no bulk outflows, very high metallicity, very high density of the warm neutral medium and a low density and highly ionized medium) that are unlikely to exist in any real ISM.

Secondly, as a consequence of simulating cosmological volumes we are unable to resolve the ISM of the individual galaxies to be able to model the Lyα line profile that emerges out of any galaxy. We have therefore assumed the emergent Lyα line to have a Gaussian profile with the width being set by the rotation velocity of the galaxy. However, several observational (Tapken et al. 2007; Yamada et al. 2012) and theoretical works (Verhamme et al. 2008; Jensen et al. 2013) have found the emerging Lyα line profile to be double-peaked; this profile results in higher IGM Lyα transmission values compared to a Gaussian profile (Jensen et al. 2013). An increase in T_α due to such a double-peaked profile allows our theoretical LFs to fit the observations with slightly lower f_α/f_c values.

Thirdly, we assume a constant escape fraction $f_{\rm esc}$ for all galaxies. Although the value of $f_{\rm esc}$ and its dependence on galaxy properties (such as the stellar mass) are only poorly known, recent work hints at an $f_{\rm esc}$ that decreases with increasing mass (Ferrara & Loeb 2013; Paardekooper et al. 2011). If $f_{\rm esc}$ is indeed higher for low-mass galaxies, the ionization topology would become more homogeneous with the H II regions being built by low-mass (high-mass) galaxies being larger (smaller) than the constant $f_{\rm esc}$ case. This would have two effects: on the one hand the IGM Lyα transmission would be enhanced (decrease) for low-mass (high-mass) galaxies, leading to a steeper Lyα LF. On the other hand, due to its direct dependence on $f_{\rm esc}$, the intrinsic Lyα luminosity would decrease (increase) for low-mass (high-mass) galaxies, leading to a flattening of the Lyα LF. The relative importance of these two effects is the subject of a work currently in preparation.

Fourthly, we assume that dust in high-redshift galaxies is solely produced by type II supernovae. However, as shown by Valiante et al. (2009), AGB stars can start contributing to significantly, and even dominate, the dust budget in regions of very high star formation (e.g. QSO/quasars) after $150 - 500$ Myrs. However, a significant part of this extra dust could be destroyed by forward SN shocks (Bianchi & Schneider 2007) that have also not been considered in this work.

In ongoing calculations, our aim is to see whether the parameter space allowed by "clumped" dust can be narrowed with a combination of LAE clustering and through 21cm brightness maps that will be directly testable with upcoming observations with the Subaru Hyper-Suprime Camera and LoFAR.

ACKNOWLEDGMENTS

The authors thank the referee M. Dijkstra for his insightful and constructive comments, Gustavo Yepes for providing the hydrodynamical simulation and Benedetta Ciardi for a collaboration in developing pCRASH. This work has been performed under the HPC-EUROPA2 project (project number: 228398) with the support of the European Commission - Capacities Area - Research Infrastructures. AH thanks the European trans-national HPC access programme for a 8-week visit to the Institute of Astronomy (Edinburgh) where a part of this work was carried out. PD acknowledges the support of the European Research Council. The hydrodynamical simulation has been performed on the Juropa supercomputer of the Jülich Supercomputing Centre(JSC).

REFERENCES

Barkana R., Loeb A., 2001, Phys. Rep., 349, 125
Barnes J., Efstathiou G., 1987, ApJ, 319, 575
Bate M. R., Burkert A., 1997, MNRAS, 288, 1060
Bertoldi F., Cox P., 2002, A&A, 384, L11
Bianchi S., Schneider R., 2007, MNRAS, 378, 973
Biffi V., Maio U., 2013, MNRAS, 436, 1621

Bouwens R. J., Illingworth G. D., Franx M., Ford H., 2007, ApJ, 670, 928
Bouwens R. J. et al., 2011, ApJ, 737, 90
Bradley L. D. et al., 2012, ApJ, 760, 108
Choudhury T. R., Ferrara A., 2007, MNRAS, 380, L6
Ciardi B., Ferrara A., 2005, Space Sci. Rev., 116, 625
Ciardi B., Ferrara A., Marri S., Raimondo G., 2001, MNRAS, 324, 381
Cole S., Lacey C. G., Baugh C. M., Frenk C. S., 2000, MNRAS, 319, 168
Curtis-Lake E. et al., 2012, MNRAS, 422, 1425
Dayal P., Dunlop J. S., Maio U., Ciardi B., 2013, MNRAS, 434, 1486
Dayal P., Ferrara A., 2012, MNRAS, 421, 2568
Dayal P., Ferrara A., Gallerani S., 2008, MNRAS, 389, 1683
Dayal P., Ferrara A., Saro A., 2010, MNRAS, 402, 1449
Dayal P., Ferrara A., Saro A., Salvaterra R., Borgani S., Tornatore L., 2009, MNRAS, 400, 2000
Dayal P., Maselli A., Ferrara A., 2011, MNRAS, 410, 830
Dijkstra M., Lidz A., Wyithe J. S. B., 2007, MNRAS, 377, 1175
Dijkstra M., Mesinger A., Wyithe J. S. B., 2011, MNRAS, 414, 2139
Duval F., Schaerer D., Östlin G., Laursen P., 2014, A&A, 562, A52
Dwek E., Galliano F., Jones A. P., 2007, ApJ, 662, 927
Ferrara A., Loeb A., 2013, MNRAS, 431, 2826
Ferrara A., Pettini M., Shchekinov Y., 2000, MNRAS, 319, 539
Finkelstein S. L., Rhoads J. E., Malhotra S., Grogin N., 2009, ApJ, 691, 465
Forero-Romero J. E., Yepes G., Gottlöber S., Knollmann S. R., Cuesta A. J., Prada F., 2011, MNRAS, 415, 3666
Fujita A., Martin C. L., Mac Low M.-M., Abel T., 2003, ApJ, 599, 50
Gnedin N. Y., Kravtsov A. V., Chen H.-W., 2008, ApJ, 672, 765
González V., Labbé I., Bouwens R. J., Illingworth G., Franx M., Kriek M., 2011, ApJ, 735, L34
González V., Labbé I., Bouwens R. J., Illingworth G., Franx M., Kriek M., Brammer G. B., 2010, ApJ, 713, 115
Haardt F., Madau P., 1996, ApJ, 461, 20
Hansen M., Oh S. P., 2006, MNRAS, 367, 979
Hu E. M., Cowie L. L., Barger A. J., Capak P., Kakazu Y., Trouille L., 2010, ApJ, 725, 394
Iliev I. T., Shapiro P. R., McDonald P., Mellema G., Pen U.-L., 2008, MNRAS, 391, 63
Iye M. et al., 2006, Nature, 443, 186
Jensen H., Laursen P., Mellema G., Iliev I. T., Sommer-Larsen J., Shapiro P. R., 2013, MNRAS, 428, 1366
Kashikawa N. et al., 2006, ApJ, 648, 7
Kashikawa N. et al., 2011, ApJ, 734, 119
Knollmann S. R., Knebe A., 2009, ApJS, 182, 608
Komatsu E. et al., 2009, ApJS, 180, 330
Labbé I. et al., 2010a, ApJ, 716, L103
Labbé I. et al., 2010b, ApJ, 708, L26
Labbé I. et al., 2013, ApJ, 777, L19
Laursen P., Duval F., Östlin G., 2013, ApJ, 766, 124
Laursen P., Sommer-Larsen J., Razoumov A. O., 2011, ApJ, 728, 52
Ledoux C., Bergeron J., Petitjean P., 2002, A&A, 385, 802
Leitherer C. et al., 1999, ApJS, 123, 3
Maio U., Khochfar S., Johnson J. L., Ciardi B., 2011, MNRAS, 414, 1145
Maiolino R. et al., 2006, Mem. Soc. Astron. Italiana, 77, 643
Malhotra S. et al., 2005, ApJ, 626, 666
Maselli A., Ciardi B., Kanekar A., 2009, MNRAS, 393, 171
Maselli A., Ferrara A., Ciardi B., 2003, MNRAS, 345, 379
McLure R. J., Cirasuolo M., Dunlop J. S., Foucaud S., Almaini O., 2009, MNRAS, 395, 2196
McLure R. J. et al., 2013, MNRAS, 432, 2696
McLure R. J., Dunlop J. S., Cirasuolo M., Koekemoer A. M., Sabbi E., Stark D. P., Targett T. A., Ellis R. S., 2010, MNRAS, 403, 960
McLure R. J. et al., 2011, MNRAS, 418, 2074
McQuinn M., Hernquist L., Zaldarriaga M., Dutta S., 2007a, MNRAS, 381, 75
McQuinn M., Lidz A., Zahn O., Dutta S., Hernquist L., Zaldarriaga M., 2007b, MNRAS, 377, 1043
Miralda-Escude J., 1998, ApJ, 501, 15
Mitra S., Ferrara A., Choudhury T. R., 2013, MNRAS, 428, L1
Mo H. J., Mao S., White S. D. M., 1998, MNRAS, 295, 319
Nagamine K., Ouchi M., Springel V., Hernquist L., 2010, PASJ, 62, 1455
Neistein E., Dekel A., 2008, MNRAS, 383, 615
Neufeld D. A., 1991, ApJ, 370, L85
Oesch P. A. et al., 2010, ApJ, 709, L16
Omont A., Cox P., Bertoldi F., McMahon R. G., Carilli C., Isaak K. G., 2001, A&A, 374, 371
Orsi A., Lacey C. G., Baugh C. M., Infante L., 2008, MNRAS, 391, 1589
Osterbrock D. E., 1989, Astrophysics of gaseous nebulae and active galactic nuclei
Ouchi M. et al., 2009, ApJ, 706, 1136
Ouchi M. et al., 2010, ApJ, 723, 869
Paardekooper J.-P., Pelupessy F. I., Altay G., Kruip C. J. H., 2011, A&A, 530, A87
Partl A. M., Maselli A., Ciardi B., Ferrara A., Müller V., 2011, MNRAS, 414, 428
Pentericci L. et al., 2011, ApJ, 743, 132
Pettini M., Smith L. J., Hunstead R. W., King D. L., 1994, ApJ, 426, 79
Raičević M., Theuns T., 2011, MNRAS, 412, L16
Razoumov A. O., Sommer-Larsen J., 2006, ApJ, 651, L89
Razoumov A. O., Sommer-Larsen J., 2010, ApJ, 710, 1239
Ricotti M., Shull J. M., 2000, ApJ, 542, 548
Salpeter E. E., 1955, ApJ, 121, 161
Salvaterra R., Ferrara A., Dayal P., 2011, MNRAS, 414, 847
Salvaterra R., Maio U., Ciardi B., Campisi M. A., 2013, MNRAS, 429, 2718
Samui S., Srianand R., Subramanian K., 2009, MNRAS, 398, 2061
Santos M. R., 2004, MNRAS, 349, 1137
Scarlata C. et al., 2009, ApJ, 704, L98

Schaerer D., de Barros S., 2010, A&A, 515, A73
Sheth R. K., Tormen G., 1999, MNRAS, 308, 119
Shimasaku K. et al., 2006, PASJ, 58, 313
Sobacchi E., Mesinger A., 2013, MNRAS, 432, 3340
Springel V., 2005, MNRAS, 364, 1105
Springel V., Hernquist L., 2003, MNRAS, 339, 289
Stark D. P., Ellis R. S., Bunker A., Bundy K., Targett T., Benson A., Lacy M., 2009, ApJ, 697, 1493
Stark D. P., Ellis R. S., Chiu K., Ouchi M., Bunker A., 2010, MNRAS, 408, 1628
Stark D. P., Schenker M. A., Ellis R., Robertson B., McLure R., Dunlop J., 2013, ApJ, 763, 129
Steinmetz M., Bartelmann M., 1995, MNRAS, 272, 570
Stratta G., Maiolino R., Fiore F., D'Elia V., 2007, ApJ, 661, L9
Sutherland R. S., Dopita M. A., 1993, ApJS, 88, 253
Taniguchi Y. et al., 2005, PASJ, 57, 165
Tapken C., Appenzeller I., Noll S., Richling S., Heidt J., Meinköhn E., Mehlert D., 2007, A&A, 467, 63
Todini P., Ferrara A., 2001, MNRAS, 325, 726
Valiante R., Schneider R., Bianchi S., Andersen A. C., 2009, MNRAS, 397, 1661
Verhamme A., Schaerer D., Atek H., Tapken C., 2008, A&A, 491, 89
Verhamme A., Schaerer D., Maselli A., 2006, A&A, 460, 397
Wise J. H., Cen R., 2009, ApJ, 693, 984
Wyithe J. S. B., Loeb A., 2013, MNRAS, 428, 2741
Yabe K., Ohta K., Iwata I., Sawicki M., Tamura N., Akiyama M., Aoki K., 2009, ApJ, 693, 507
Yajima H., Choi J.-H., Nagamine K., 2011, MNRAS, 412, 411
Yamada T., Matsuda Y., Kousai K., Hayashino T., Morimoto N., Umemura M., 2012, ApJ, 751, 29
Zheng Z., Cen R., Trac H., Miralda-Escudé J., 2010, ApJ, 716, 574

APPENDIX A: COMPARING THE SIMULATIONS WITH LBG OBSERVATIONS

A1 Stellar mass functions and stellar mass density

We build simulated LBG mass functions by summing up LBGs on the basis of their stellar mass, and dividing this by the width of the bin and the simulated volume; for consistency with observations, this calculation is carried out for all LBGs with $M_{UV} \leqslant -18$. As expected from the hierarchical model, small mass systems are the most numerous, with the number density decreasing with increasing mass. Further, the mass function shifts to progressively lower masses with increasing redshifts, as fewer massive systems have had the time to assemble. Both trends can be seen clearly from Fig. A1: at $z \simeq 6$, galaxies with $M_* \simeq 10^{8.5}\mathrm{M}_\odot$ are two orders of magnitude more numerous as compared to more massive galaxies with $M_* \simeq 10^{10.5}\mathrm{M}_\odot$. Secondly, while there are systems as massive as $10^{10.7}\mathrm{M}_\odot$ in the simulated volume at $z \simeq 6$, such systems had not the time to evolve by $z \simeq 8$ where the most massive systems have $M_* \simeq 10^{9.4}\mathrm{M}_\odot$. From

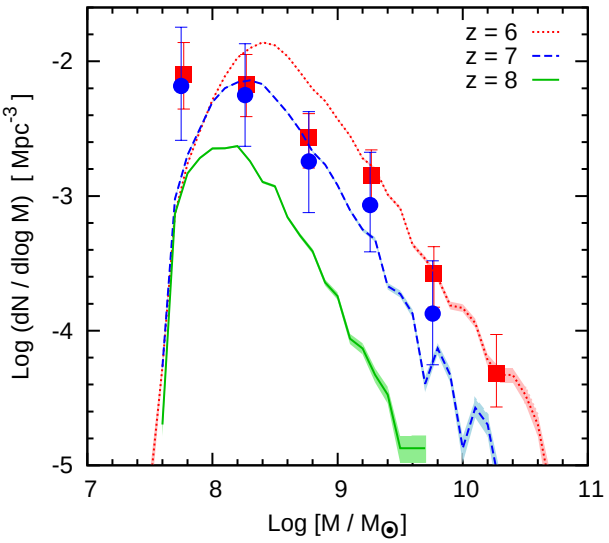

Figure A1. Stellar mass function for LBGs with $M_{UV} \leqslant -18$ at $z \simeq 6-8$. The dotted (red), dashed (blue) and solid (green) lines represent the simulated stellar mass functions for $z \simeq 6, 7$ and 8, respectively. The shaded areas denote the respective Poisson errors. Squares (circles) represent the observational stellar mass functions at $z \simeq 6$ (7) inferred by González et al. (2011), corrected for completeness but not for dust.

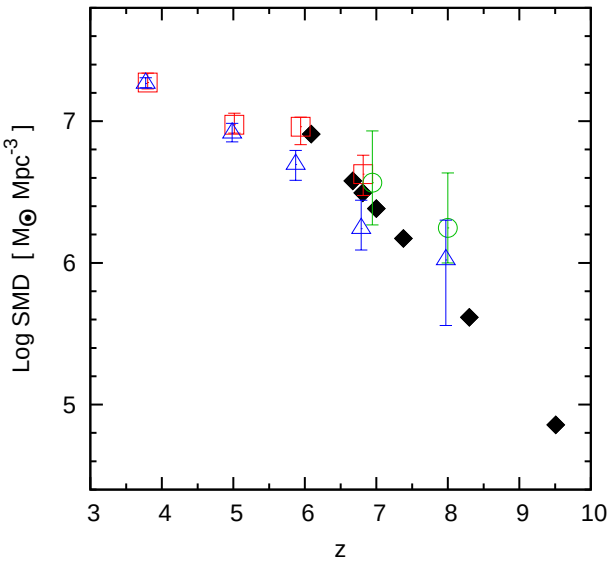

Figure A2. Total stellar mass density for LBGs with $M_{UV} \leqslant -18$. Filled black points represent the simulated SMDs; Poissonian errors are too small to be visible on the plot. The other symbols show the observed SMD values inferred by González et al. (2011, empty red squares), Labbé et al. (2010a, empty green circles), Labbé et al. (2010b, empty green circles), Stark et al. (2013, empty blue triangles).

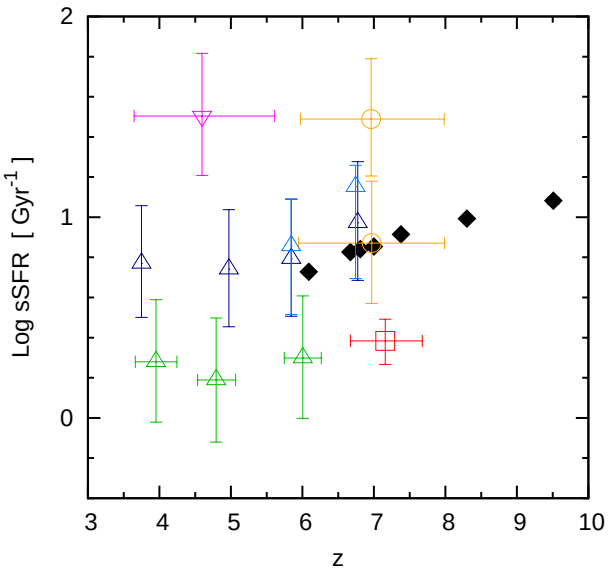

Figure A3. Specific star formation rate for LBGs with $M_{UV} \leqslant -18$. Filled black points represent the simulated sSFRs; Poissonian errors are too small to be visible on the plot. Observed sSFR values plotted have been taken from: González et al. (2010, empty red squares), Stark et al. (2009, empty green triangles), Yabe et al. (2009, empty magenta triangles), Schaerer & de Barros (2010, empty orange circles), Stark et al. (2013, empty blue triangles).

the same figure, we see that the slope and amplitude of the simulated stellar mass functions are in agreement with the observations for $M_* \geqslant 10^{7.5}\mathrm{M}_\odot$; this number marks the limit of our simulation resolution for galaxies containing at least 4N gas particles and 10 star particles, as a result of which, the number density drops below it.

As a result of the stellar mass functions shifting to progressively lower masses and number densities with increasing redshift (see Fig. A1), the total SMD in the simulated volume decreases with increasing redshift, as shown in Fig. A2, falling by a factor of about 40 from $10^7\mathrm{M}_\odot\,\mathrm{Mpc}^{-3}$ at $z \simeq 6$ to $10^{5.4}\mathrm{M}_\odot\,\mathrm{Mpc}^{-3}$ at $z \simeq 9.5$. As expected from the agreement between the simulated stellar mass functions and those inferred observationally by González et al. (2011), the simulated SMD values are also in agreement with the observations. However, as pointed out by Schaerer & de Barros (2010) and Stark et al. (2013), including the effects of nebular emission can lead to a decrease in the observationally inferred stellar mass values; this effect causes a slight discrepancy between the SMD values obtained from our model, and those inferred by Stark et al. (2013) at $z \simeq 6$, as shown in Fig. A2.

A2 Specific star formation rates

The specific star formation rate (sSFR) is an excellent indicator of the current SFR compared to the entire past star formation history of the galaxy. This quantity also has the advantage that it is relatively independent of assumptions regarding the IMF, metallicity, age and dust content since both the SFR and stellar mass are affected similarly by these parameters. Recently, a number of observational groups have suggested that the sSFR settles to a value consistent with $2-3\,\mathrm{Gyr}^{-1}$ at $z \simeq 3-8$ (Stark et al. 2009; González et al. 2010; McLure et al. 2011; Labbé et al. 2013; Stark et al. 2013). This result is quite surprising given that theoretically, the sSFR is expected to trace the baryonic infall rate that scales as $(1+z)^{2.25}$ (Neistein & Dekel 2008). However, Labbé et al. (2013) and Stark et al. (2013) have shown that at least a part of this discrepancy can be accounted for by the addition of nebular emission lines; indeed, the sSFR can rise by a factor of about 5 between $z \simeq 2$ and $z \simeq 7$ when nebular emission is taken into account.

Physically, the least massive galaxies tend to have the highest sSFR: as a result of their low M_* values, even a small amount of SF can boost their sSFR compared to that of more massive systems (see also Dayal & Ferrara 2012; Dayal et al. 2013). Since the mass function progressively shifts to lower masses with increasing redshifts, and smaller mass galaxies have larger sSFR values, the sSFR rises with increasing redshift, from $sSFR \simeq 5\,\mathrm{Gyr}^{-1}$ at $z \simeq 6$ to $sSFR \simeq 12\,\mathrm{Gyr}^{-1}$ at $z \simeq 9.5$, in accordance with other theoretical results (Dayal et al. 2013; Biffi & Maio 2013; Salvaterra et al. 2013). We note that in the redshift range of overlap ($z \simeq 6-7$), the theoretically inferred sSFR values are in agreement with observations.

APPENDIX B: COSMIC VARIANCE

In Fig. A4 we show the cosmic variance associated with the simulated Lyα LFs. The cosmic variance is estimated by computing the Lyα LFs for 8 sub-volumes of our simulation volume, such that each sub-volume is 1.87×10^5 Mpc^3 and thus comparable to the volume observed by Kashikawa et al. (2011). As $\langle\chi_{HI}\rangle$ evolves from an IGM which is predominantly neutral at $\langle\chi_{HI}\rangle \simeq 0.75$ to one wherein reionization is complete ($\langle\chi_{HI}\rangle \simeq 10^{-4}$), the value of T_α increases in all sub-volumes, leading to a decrease in the cosmic variance at the faint-end of the LF; the variance at the bright-end arises due to few objects being massive/luminous enough to occupy these bins in any given sub-volume.

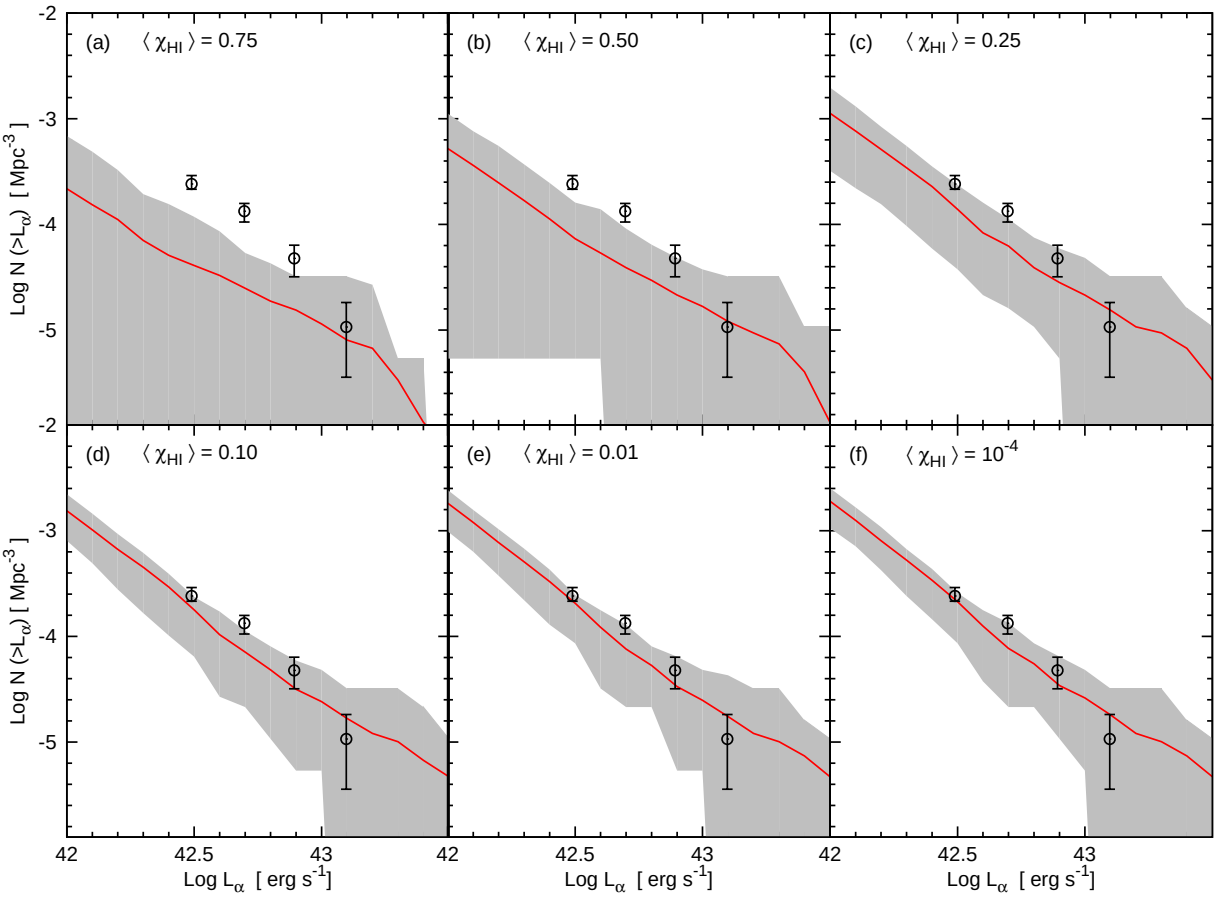

Figure A4. Simulated cumulative Lyα LFs and the associated cosmic variance for homogeneous dust ($f_\alpha/f_c = 0.68$) and $f_{\rm esc} = 0.05$. The panels show the results for different neutral hydrogen fractions, $\langle \chi_{HI} \rangle \simeq 0.90$, 0.75, 0.50, 0.25, 0.10, 0.01, 10^{-4}, as marked. In each panel, the solid red line shows the Lyα LF for the whole simulation box of volume $(80h^{-1}{\rm Mpc})^3$ with the gray shaded areas showing the associated cosmic variance obtained by splitting the entire simulation box into 8 equal sub-volumes. In each panel, the open circles show the Lyα LFs at $z \simeq 6.5$ observed by Kashikawa et al. (2011). As the IGM becomes more ionized, the value of T_α increases in all sub-volumes, leading to a decrease in the cosmic variance at the faint-end of the LF; the variance at the bright-end arises due to the low numbers of massive galaxies found in any given sub-volume.